UiT
THE ARCTIC
UNIVERSITY
OF NORWAY

Faculty of Science and Technology
Department of Physics and Technology

Cross-Phase Based Multi-Camera Video Synchronization Calibration with Sub Frame Rate Accuracy

Design, build and testing of a new calibration system
—

Pavithiran Sivasothy
FYS-3931 Master's thesis in Space physics, June 2020

Abstract

In auroral research, it is necessary to accurately measure the time-shift differences between varying light sources. Such measurements can be carried out using two or more digital cameras, or between different regions of an image obtained using a single camera. An example of this is measurements of the time-shifts between prompt auroral emissions originating from different altitude regions during pulsating or flickering aurora, which can give information about auroral electron transport and its chemical compositions. Such measurements require a camera synchronization with an accuracy better than the time delay.

In this thesis, a calibration technique was developed to simulate the time-shifts, and a cross-phase based method was later used to estimate the time-shift, with sub-frame rate precision being designed and tested. This method is based on analyzing the frequency variance of the cross-phase between time-shifted signals. The results showed that with time-series with 60 fps, it is possible to measure the time-shifts as small as 500 μs accuracy, and with a time delay uncertainty better than 10 μs. The calibration technique was developed to enable measurements of electron transport related to optical emission time differences with high frame rate auroral imaging systems, but the technique can also be applied to a broad range of other applications - such as camera timing calibrations. The calibration technique met the design requirements, and further demonstrated that time-shifts much smaller than the frame rate can be determined.

Acknowledgements

Contents

List of Figures

List of Tables

List of Symbols

Δt Pixel readout time

τ Time-delay

σ_τ Time-delay-uncertainty

$I_1(t)$ Intensity of light source 1

$I_2(t)$ Intensity of light source 2

ω Frequency

$\boldsymbol{\gamma}$ Intensity scaling factor

ϕ Phase

1

Introduction

Perfect multi-camera synchronization have long been a difficult task to achieve. The ideal synchronization would be no time delay between the image-stream from the cameras, and completely without synchronization uncertainty. For optical observations of the aurora, sufficient synchronization requirements have traditionally been taken as some small fraction of the frame rate (which have typically been either ~0.1 - 1 frames-per-second (fps)), which have technically been met by GPS pulse-per-second signal for timing synchronization.

Multi-camera synchronization is essential for many fields of work. Low synchronization uncertainty is important in diverse fields such as multimedia streaming services to gain low to no latency and to scientific research such as auroral studies. For rapid auroral research, it is imperative to have small synchronization error, at the best case, between 1 ms and 100 μs. For this thesis, a synchronization uncertainty between 1 ms and 500 μs was the expressed target. In order to achieve this, an aurora was simulated, recorded and the offsets between the time-series for different image regions was estimated.

High speed optical observations of aurora have typically been limited by video frame-rates of approximately 25-50 fps. The reasonable synchronization-requirement for auroral observations would be 5 ms. The $O(^1S)$ atom is the main source of the auroral green line that can be observed. $O(^1S)$ has many sources in the terrestrial thermosphere; energy transfer from $N_2(A)$, direct electron impact of O, photodissociation of O_2 and dissociative recombination of O_2^+ with N. The effective lifetime of the $O(^1S)$ is 0.7 s which leads to a

time-shift relative to prompt emissions on the order if 0.1 s, which can be confirmed with observations with recent time-dependent electron-transport calculations done by Gustavsson (2020), who predicted that there should be time-shifts between prompt emissions during periods of aurora that varies at frequencies higher than 5 Hz. Examples of such phenomena are: flickering aurora (e.g. Whiter et al., 2010; Sakanoi and Fukunishi, 2004), auroral curls (e.g. Trondsen and Cogger, 1998; Vogt et al., 1999; Lanchester et al., 1997), and other dynamic smaller-scale auroras (e.g. Dahlgren et al., 2010; Semeter and Blixt, 2006). These time shifts are due to finite velocity of pulses of precipitating electrons propagating down in altitude, which cause prompt auroral emission from different characteristic altitude regions with milliseconds time scale differences.

In rapidly varying auroras there might be time shift between prompt emission in the order of 1 to 10 ms. To accurately estimate time-shifts on such short time scales, a camera synchronization error in the order of 100 to 500 μs is required. With this in mind, the multi-camera synchronization method described in this thesis aims to contribute to a simple and robust method to determine camera-synchronization with that accuracy. In fast moving auroras on the 90 to 150 km altitude, it is even more difficult as pixels in the cameras might not even correlate with the other cameras in a multi-camera system. Such a small synchronization error is required as the delay between the 4278 Å and 6370 Å, 7774 Å and 8556 Å emissions are 10, 5 and 3 ms respectively. To accurately attribute the observed time delay, τ, to the time-shift in the auroral emission it is therefore important to have small synchronization uncertainty between the cameras.

The time-shifts between the different emissions should be detectable with multi-monochromatic high-speed imaging - provided that the camera synchronization have better accuracy than $\sim$ 100 μs (Gustavsson, 2020). Resolving these small time-shifts requires simultaneous observations of multiple auroral emissions with synchronization accuracy known to be better than 1 ms uncertainty, and preferable, better than 500 - 100 μs. This is a stricter requirement than what has been achieved in previous work, such as ground-based multispectral high-speed imaging of flickering auroras by Kataoka et al. (2011) obtained a sampling error less than 10 ms. For autonomous vehicle synchronization sequences for stereoscopic cameras of 16.7 ms was achieved by Vibeck (2015). A video-stream synchronization method conducted by Šmíd and Matas (2017) obtained a synchronization error better than 1 ms utilizing rolling shutter cameras. This part will be covered in depth in a later section.

In order to be able to measure time-shifts on a better time scale than 500 to 100 μs from multi-wavelength auroral observations, a new time-shift measurement technique is required. The objective of this thesis is to design, test

and present such a technique. The technique that has been developed is based on phase-detection of cross-spectra between image sequences of deliberately time-shifted signals. This is very similar to the radio-astronomic very long baseline interferometry, VLBI, a technique for estimating the relative time delays between different radio receiver stations and a point-like radio source (Shapiro, 1976). In order to validate this technique in practice, a calibration device capable of producing optical emission with known time delays was constructed, which allowed to estimate the accuracy of the measurements. The technique has been demonstrated a capacity to detect as small time-shifts than 500 μs with an uncertainties better than 10 μs from image-sequences taken with 60 fps

In Chapter 2 the technological background for this thesis and why this kind of camera-synchronization is relevant and previous work on the topic in the related fields and other fields is presented. The theory behind this work will be presented in Chapter 3, followed by the results and a discussion in Chapter 4. Chapter 5 summarizes the study and presents some concluding remarks and ideas for possible future work.

2

Backgroung

There are many reasons behind the chosen field of study. The primary motivation behind this thesis is to facilitate auroral research. The work of this thesis should contribute to lower the synchronization uncertainty between optical cameras while capturing fast-moving auroras with short lifetime. In addition the method might be used in other fields, such as in facilitating autonomous camera synchronization on vehicles to prevent any accidents on the road, as well as lowering the synchronization uncertainty between sound and video in streams to prevent any sound/video lag relative to each other. In this chapter, the background, the scientific motivation for this study, as well as an overview of previously conducted studies in the field of multi-camera synchronization will be presented.

2.1   Auroral Studies

The aurora borealis, or the northern lights, are the result of energetic particles, mainly electrons, precipitating down into the polar atmosphere from the magnetosphere. The energetic electrons and protons result from the interactions between the solar wind and the magnetosphere. The sun ejects particles which interact with the magnetosphere of the Earth, where a chain of poorly understood processes leads to precipitation of high energetic electrons and protons. The high energy particles collide with the atoms and molecules in the thermosphere and cause ionization, producing secondary electrons with low

energies up to about ~100 eV. The secondary electrons are then the dominant cause of the electron impact excitation. Auroras are the following emissions of photons in the upper atmosphere.

2.2   Why spectroscopy is important for Auroral studies

Spectroscopy was already fundamental at the start of scientific auroral studies. When spectroscopic measurements were analyzed, the green line was found to be the dominant emission, especially in high-altitude auroras. Anders Johan Ångström was the first to observe the green line through spectroscopy in 1868. Before Ångström's work, only visual studies of the auroral colors had been carried on. By using calcium Fraunhofer lines he determined that the wavelength of the auroral green line was 5577 Å (Henriksen and Egeland, 1988). One of the few ways to determine the source of different auroral emissions was to compare the emission lines in the auroral spectrum with spectra from laboratory experiments. Aurora in different emissions reveal information about the energy of the primary precipitation. This is primarily because the N_2 to O mixing ratio increases with decreasing altitude. This leads to a relatively larger excitation of N_2 compared to O from secondary electrons at 100 km than at 150 km. Since higher-energy electrons have their peak ionization rate at lower altitudes the ratio between N_2 and O-emissions increases with increasing energy of the primary electrons. Additional factors that comes in are the energy variation of the excitation cross-sections and for the forbidden emissions (e.g. 5577 Å and 6300 Å), both the long radiative life-time and quenching has to be accounted for.

2.3   Recent Auroral studies

Auroral multi-camera synchronization is the main purpose of this thesis. Additionally, it is important to have low synchronization uncertainty between the optical cameras - primarily to determine the time differences between prompt emissions, and secondarily to properly study the chemical composition in the aurora, which has been difficult to do earlier.

Ground-based multi spectral high-speed imaging of flickering aurora, with the objective to experiment the dispersive Alfven waves acceleration was conducted by Kataoka et al. (2011). For camera synchronization they used artificial flashes of a light emitting diode synchronized with GPS-signal, where it was observed

by two cameras at the same time to match the sampling time with an accuracy better than 10 ms. The synchronization error they achieved was 10 ms with 0.5 km spatial shift on average in the obtained flickering patterns at 6705 Å and 8446 Å. These emissions are sensitive to relatively hard and soft electrons. The cameras they used were one Hammamatsu EMCCD camera and one Andor iXon EMMCD camera. With the use of two different cameras there might be some uncertainties about how simultaneous the actual exposure of the triggering are (Kataoka et al., 2011).

2.4   Recent Studies

Multi-camera synchronization is also a requirement in other fields of work, such as for autonomous vehicle navigation in traffic and multi-camera synchronization at different angles in sports video-streams, and consumer use of general camera synchronization. In this section, a review of previous multi-camera synchronization techniques in other fields of work will be presented.

A solution for solving the rolling shutter shear and the synchronization problem at the same time was presented by Bradley et al. (2009) for consumer video camera arrays. They presented two different methods to solve the problem. The first method performs optical synchronization by using strobe illumination. Strobe lights creates simultaneous exposure images for all cameras that can be used for synchronization. The second approach works in situations such as outdoor scenes, where strobe lights are impractical. This method removes the rolling shutter shear by applying a warp along optical flow vectors to generate instantaneous images for a given sub frame portion. For synchronization of multiple cameras, it was assumed that the same video standard, i.e. that the frame duration, the total number of scan lines per frame, and the number of visible scan lines would be identical for all cameras, and that either all or none of the cameras would be interlacing. Interlacing happens when cameras trade spatial for temporal resolution by recording the even and odd scan lines in separate fields. Stroboscopes have for long been used for obtaining instantaneous exposures of moving objects using standard cameras without rolling shutter. An extension of this approach results in multiple video streams that are optically synchronized through illumination (Bradley et al., 2009).

A project to build a synchronization setup for a multi-camera system using the RayTrix digital cameras was proposed by Vibeck (2015). For their project, the synchronization requirement was better than 10 ms, but the experiment that was conducted with the flash clock was not accurate enough, such that further work had to be done. A flash clock for the hardware trigger was used, but as the flash clock only had millisecond resolution and the screen that was used

could not show images that changed faster than 16.7 ms, it was not possible to measure with better accuracy than this time span. The goal of Vibeck (2015) project was to develop a research platform for autonomous heavy duty vehicles. The two techniques that were implemented were: 1) hardware trigger, where the cameras were externally triggered by using the hardware in an external micro-controller to produce the trigger signal, and 2) two software triggers, where the camera were triggered internally by multi camera software. For the first software trigger, the first camera was ahead of the second camera, making it unable to measure any synchronization. For the second software trigger, it was stated that it was hard to trigger two cameras at an exact interval. Vibeck also has 10 ms delay in the cameras (Vibeck, 2015).

A video-stream synchronization method with precision better than 1 ms utilizing rolling shutter cameras has been developed by Šmíd and Matas (2017). They managed to obtain a time difference of 0.3 to 0.5 ms of synchronized time events. They validated the synchronization method by interpolating a puck position between two frames in the first camera and compared it against the "real" position in a second camera. To correctly model the sub-frame accurate synchronization transformation, it was required to record missing frames, different frame rates, a drift of image sensors clock and take hidden dark rows in image sensors into account. They claimed that the method is applicable to any number of rolling shutter cameras. They approached by exploiting the rolling shutter sensor property such that every sensor row started its exposure with a small relative to the onset of the neighbouring row The method that Šmíd and Matas (2017) introduced did not require an overlapping field of view and the cameras could be heterogeneous with different frame rates and resolutions. Additionally, the method could utilize frame time-stamp which make it robust to frame dropping. However, the inputs for the synchronization algorithm were frame timestamps extracted from video files or network streams and detected transition edges of abrupt lighting changes. Abrupt lighting changes are trivially detectable and are suitable for sub-frame synchronization with rolling shutter sensors, where the only requirement is that the majority of the observed scene receives light from the source (Šmíd and Matas, 2017).

These methods are not directly applicable for the calibration system in this thesis, as there are no certain discrete events to synchronize cameras with rolling-shutter-effect-methods in auroral imaging.

3

Theory and Method

In this section, the theory, mainly the Fourier transform will be outlined, followed by the method behind the idea of the camera calibration technique. Lastly, the design and the measurements of the calibration will be presented.

3.1 Theory

The spectral components of a signal $X(\omega)$ of the function $x(t)$ can be represented by the Fourier Transform:

$$\hat{X}(\omega) = \int_{-\infty}^{\infty} x(t)e^{i\omega t}dt = x(t) = \int_{-\infty}^{\infty} \hat{X}(\omega)e^{i\omega t}d\omega \qquad (3.1)$$

$|X(\omega)|$ is the amplitude of $x(t)$. When there is a signal with a slight time delay can be written as:

$$\hat{X}_1(\omega) = a(\omega)e^{i\omega t}\exp^{i\phi}$$
$$\hat{X}_2(\omega) = a(\omega)e^{i\omega(t-\tau)}e^{i\phi}$$
$$\hat{X}_1(\omega)\hat{X}_2^*(\omega) = |a(\omega)|^2 e^{i\omega\tau}.$$

The phase angle between $\hat{X}_1$ and $\hat{X}_2^*$ can then be calculated by

$$\angle\hat{X}_1\hat{X}_2^* = \omega\tau \qquad (3.2)$$

where τ is the time delay. Cross spectral analysis allows for the determination of this time delay between two time series as a function of frequency.

3.2 Method

The idea and method behind the calibration system is presented in this section. The idea behind the synchronization device is to take two time-varying intensities $I_1(t)$ and $I_2(t)$, where $I_2(t)$ is a time delayed version of $I_1(t)$. If their intensities are related to one another and follows the relationship: $I_2(t) = \gamma I_1(t - \tau)$, where γ is a scaling factor, then it is possible to determine the time delay, τ. The second light source is therefore a time-shifted and scaled version of the first light source. The Fourier transform of these functions will give the relationship between the time delay and phase shift in the frequency domain:

$$\hat{I}_1(\omega) = \int_{-\infty}^{\infty} I_1(t) e^{-i\omega t} dt. \tag{3.3}$$

$$\hat{I}_2(\omega) = \int_{-\infty}^{\infty} \gamma I_1(t) e^{-i\omega(t-\tau)} dt. \tag{3.4}$$

and with the relationship between these signals and taking the complex conjugated of the signals that is received

$$\hat{I}_2(\omega) = \gamma e^{i\omega\tau} \int_{-\infty}^{\infty} I_1(t - \tau) e^{-i\omega(t-\tau)} dt = \gamma e^{i\omega\tau} \hat{I}_1(\omega). \tag{3.5}$$

If the cross-spectrum of $I_1(t)$ and $I_2(t)$ is calculated, one can see that the phase depends on the time delay τ. It is then possible to assume that $I_1(t)$ and $I_2(t)$ have uncorrelated random noise. The mean cross-spectra of the two signals can therefor be represented as

$$E\{\hat{I}_1(\omega)\hat{I}_2^*(\omega)\} = \gamma e^{i\omega\tau} E\{|\hat{I}_1(\omega)|^2\}. \tag{3.6}$$

The phase-angle, ϕ, of the mean cross-spectrum components are therefore linearly dependent on time delay and can be represented on the same form as Equation 3.2:

$$\angle E\{\hat{I}_1(\omega)\hat{I}_2^*(\omega)\} = \phi_{12}(\omega) = \omega\tau. \tag{3.7}$$

Thus, the phase of the mean cross-spectrum of two image pixels that measure the different time-shifted intensity time-series will provide information about the relative time delay between signals recorded by these two image pixels. The estimation of the Fourier transforms of the discretized signals are representing the intensity of two image pixels that measure $I_1(t)$ and $I_2(t)$ using discrete Fourier transform (DFT). The pixel readout time is constant over time, making

it possible to reduce noise by averaging multiple measurement of the cross-spectrum. By increasing the length of the time-span of the observation it is possible to fit an estimate of the phase from N cross-spectral components as a function of frequency. Since equation 3.7 is valid for all frequencies, the equations for cross-phase can be combined at a range of frequencies. Equation 3.9 can therefore be written as a representation of Equation 3.8. This is done by the least-squares estimates:

$$\boldsymbol{x} = \mathbf{A}\tau + \boldsymbol{\xi} \tag{3.8}$$

$$\begin{bmatrix} \phi_{12}(\omega_1) \\ \phi_{12}(\omega_2) \\ \vdots \\ \phi_{12}(\omega_N) \end{bmatrix} = \begin{bmatrix} \omega_1 \\ \omega_2 \\ \vdots \\ \omega_N \end{bmatrix} \tau + \begin{bmatrix} \xi_1 \\ \xi_2 \\ \vdots \\ \xi_N \end{bmatrix}. \tag{3.9}$$

Where $\boldsymbol{x}$ is built up of the cross-phase measurements by the given angular frequencies, $\boldsymbol{A}$ is a matrix of angular frequencies, while the $\boldsymbol{\xi}$ is the matrix of the error of the phase. Here $\omega_1...\omega_N$ is the angular frequency, $\phi_{21}(\omega_1)...\phi_{21}(\omega_N)$ are the measurement of cross-spectral phase at the corresponding frequencies, and $\xi_1...\xi_N$ is the measurement errors. For large values of $|\omega\tau| > \pi$, it is necessary to apply phase unwrapping to the measured phase. For the high frequency, ω. It is possible to assume that the phase measurement errors are independent and normal distributed with zero mean random variables. Assuming that the errors have the same magnitude at all frequencies, $\xi_n \sim \boldsymbol{N}(0,\sigma^2)$. It is possible to obtain a maximum likelihood estimate of the time shift by using the standard linear least square estimate:

$$\hat{\tau}_{ML} = (\mathbf{A}^T\mathbf{A})^{-1}\mathbf{A}^T\boldsymbol{x}. \tag{3.10}$$

Assuming that all phase errors are identically distributed and independent, the time delay estimation error variance becomes

$$\mathrm{Var}\{\hat{\tau}_{ML}\} = \sigma_\tau^2 = \sigma^2 \mathbf{A}^T\mathbf{A}. \tag{3.11}$$

In order for this estimate to work, the magnitude of the spectral power of the light sources needs to be large enough for a sufficiently large range of frequencies. A wider bandwidth will provide a better estimate of the pixel readout time, however though frequencies above the Nyquist-frequency of the camera will lead to problems by giving aliased contributions to the lower frequencies.

3.3   Design

The cameras for the calibration system for this project consisted of optical cameras to capture the aurora, where the aurora was simulated by LED lights with varying intensity. Diffuser glasses were used to get a homogeneous spread of the LED lights such that the cameras can capture the intensities easier. The LEDs were controlled by an Arduino UNO which control both the randomness and the time-shift of the LEDs. The idea was to create varying intensity with the LEDs, resulting in a wide cross-spectra. The cross-spectra would then show how the frequency response would be for each time delay, τ, that was used. This would then be recorded in a dark environment. The design of the calibration device is shown in Figure 3.1. The device consisted of 4 main parts; green LEDs, diffuser glass, Arduino, and a smartphone camera. The whole device was easy-built and inexpensive. The cases that hold the LEDs were made of cardboard boxes with a white diffuser glass in front of it. The diffuser glasses were used to get a homogeneous spread of the LEDs. The boxes were also sealed with black duct tape to seal it from any other light sources which could interrupt the calibration device. The diffuser glasses were mainly a 600×600×4 mm, but was cut down to 155×155×4 mm to fit the window that was cut out on the cardboard boxes. The boxes were 213×172×141 mm. The LEDs were later connected to an Arduino UNO.
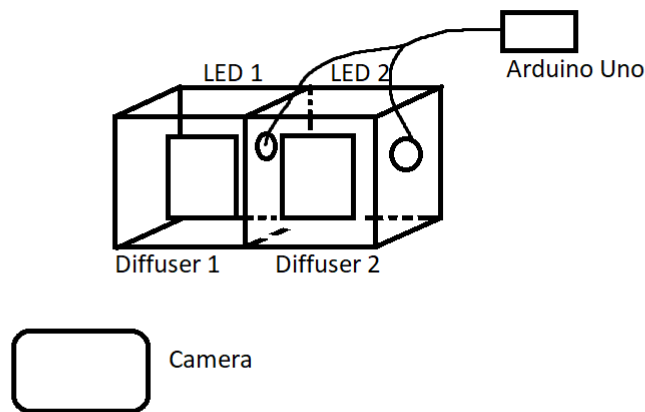

Figure 3.1: Sketch of the calibration system. Showing the cardboard boxes, camera, diffusers, LEDs, and the Arduino UNO. The diffusers are placed in a window on the front of the boxes.

The Arduino UNO was the microcontroller that produced and controlled the time delays of the light sources. The basic delay of the calibration units was set to 100 ms, while the pulse length was set to a random number between 10 and 200 ms, and the second light source was slightly time delayed with a time, τ.

The data capture of the scene with the two LEDs were executed in a dark room with a smartphone video camera at 60 fps. The smart phone was placed on a small tripod on a table to film for 10 min for each test. The setup in its whole is shown in Figure 3.2.
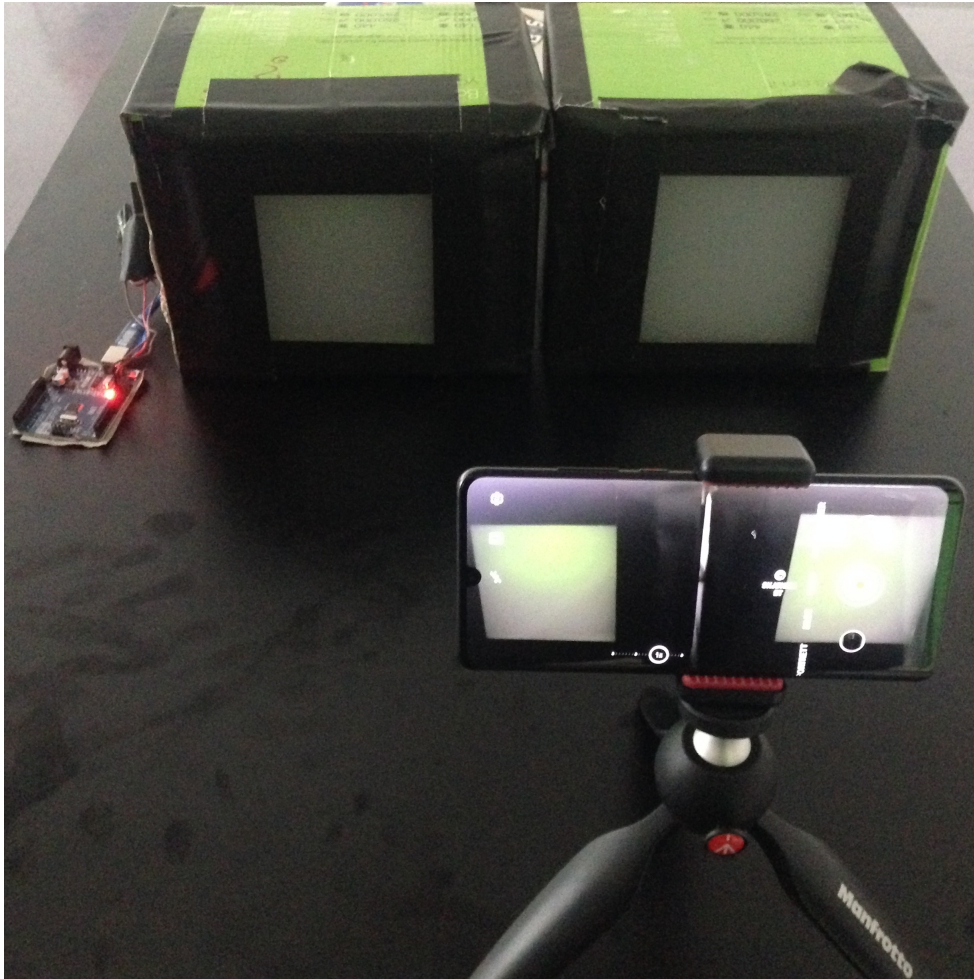

Figure 3.2: Calibration system, with the Arduino UNO to the left, cardboard boxes with the LEDs inside in the middle, and the camera phone on a tripod.

3.4 Measurements

In order to demonstrate and validate the technique for estimating relative time delays from camera time-series measurements, a calibrator device that generates two regions of relatively spatially uniform light with a time variable pseudorandom intensity and a user defined relative time shift was constructed.

The Arduino UNO was programmed to blink one LED on and off with a random pulse duration uniformly distributed between 10 and 200 ms. The randomness was used to ensure that the spectral power is distributed over a wide range of spectral components, at the same time that the power trailed off towards the edge of the spectrum. The other LED was programmed to produce the same time-series as the first LED, but with a user defined time delay.

In order to create a relatively uniform region of light, a diffuser made out of two layers of white methyl methacrylate resin. A single video frame of the device is shown in Figure 3.3
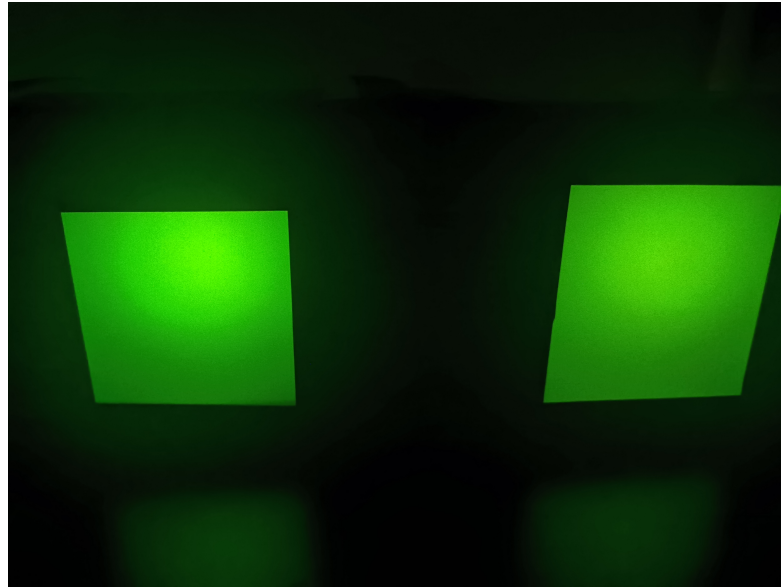

Figure 3.3: Single video frame of the calibration device. $I_1(t)$ is given on the right and the time shifted $I_2(t)$ is given oven on the left.

As a camera for recording the calibrator signal, a built-in smart phone camera on a Huawei P30 Pro was used. The video setting of this camera has a resolution of 2236x1080 pixels and an frame-rate of 60 fps. The recording were made using a tripod and stored H-264 MPEG-4 AVD format which was described in the previous section. Recording of 10 minutes of pulsating light were made at 4

different time delays, 10 ms, 2 ms, 1 ms, and 500 μs. All recordings were made in a dark room, to reduce the presence of other light sources with unknown time-variation. The test subjects were also placed on different positions relatively to one of the boxes, to test if that gave any other results. The boxes were placed at 0°, 90 °, 180 °, and 270 ° relatively to each other. Only image intensity, cross-phase, and cross-spectral power was tested for the 90° and 270°, as there was only the horizontal pixel delays that were looked at as the camera has a horizontal pixel read. Thus the time delay, τ, give higher pixel readout for each row, but the same time delay uncertainty, σ_τ.

By showing that it is possible to accurately estimate time delays as small as 500 μs between signals recorded with the same camera where the only time-shift between pixels are the pixel readout-time, it is possible to show that the time-synchronization of 2 cameras imaging one signal can be achieved with the same accuracy. While the technique and calibration device could be used to measure the time delay between two separate scientific cameras, which are driven with a shared clock, it was technically easier to demonstrate this technique using a single camera to measure the relative time delays between different pixel on the sensor.

3.5   H.264 MPEG-4 AVC

In this section I will talk briefly about the video compression method the Huawei P30 pro uses, as it is crucial for the measurements. The H.264, or Advanced Video Coding (AVC), is a video compression standard based on block-orientation motion-compensated integer-DCT-like coding. H.264 utilizes transform coding of the predicted residual. The transform applies 4×4 blocks, and instead of a discrete cosine transform (DCT), a separable integer transform with similar properties as a 4×4 DCT used. The basic transform coding process is quite similar to its predecessors. At the encoder, the process includes a forward transform, zig-zag scanning, scaling, and rounding as the quantization process followed by entropy coding. One of the main improvements of the present standard is the improved prediction process. The residual signal has less spatial correlation. This means that that a 4×4 transform is as efficient in removing correlation as a larger transformation, with similar objective compression capability. The smaller transform requires less computation and a smaller processing wordlength. As the transformation process for H.264 involves only adds and shifts, it specifies such that mismatch between encoder and decoder avoided. A quantization parameter is used for determining the quantization of transform coefficients in H.264. The quantized transform coefficients of a block are generally scanned in a zig-zag fashion and transmitted using entropy coding methods, in which entropy coding is lossless data compression Wiegand et al. (2003).

/4

Results and Discussion

In this section, the results of the measurements from the calibration device will be presented, followed by a discussion on the meaning and relevance of the results. The results will be shown in the following order: time-variation of intensity for different τ, cross-spectral power, cross-phase and time delay fits, then to validate that the time delay estimates are due to the estimated time delays there has been calculated the spatial variation of the time delay between one pixel imaging source 1 and a region of pixels imaging source 2. This makes it possible to estimate the pixel-readout-time and the line-readout-time and their respective uncertainties.

The time delays, τ, that were used for the calibration device were: 10, 2, 1, 0.5 ms. The two image intensity signal for 2.5 s of one pixel on source 1 and another pixel on source 2 is shown in Figure 4.1 and 4.2. The pixels that were chosen here are from the same row, but different pixels on the x-axis, the pixel coordinates are given in Table 4.1, where the first index is the pixels on the y-axis and the second index is the pixels on the x-axis. Using a dual channel oscilloscope, the error in the relative time delay between the two leading edges of the currents of the LEDs was determined to be less than 1 μs. The oscilloscope measurements of the currents to the LED lamps show that there are some jitters, but in overall, the signals are quite accurate making it possible to achieve good results when using LED lights as well. The results from the oscilloscope are given in Figure 4.3.

Table 4.1: Pixel areas that were used to make the measurements. For the 0° and 180° measurements, the pixels on the y-axis were the same, while the x-axis pixels were the same on the 90° and 270° measurements

time delay, τ (ms)	Rotation (degree)	Source 1 pixel (y-axis, x-axis)	Source 2 pixel (y-axis, x-axis)
10	0	(435, (445, 446))	(435, (1854, 1855))
2	0	(459, (559, 560))	(459, (2066, 2067))
1	0	(392, (535, 534))	(392, (1796, 1797))
0.5	0	(260, (500, 501))	(260, (1895, 1896))
10	90	(781, 1160)	(211, 1160)
2	90	(856, 1395)	(219, 1395)
1	90	(857, 1077)	(200, 1077)
0.5	90	(827, 1100)	(200, 1100)
1	180	(266, (560, 561))	(266, (1800, 1801))
1	270	(830, 1112)	(196, 1112)
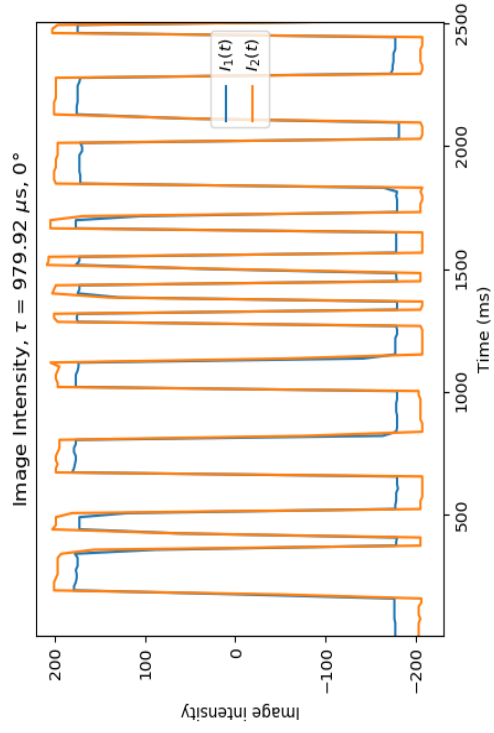
(a) Image intensity of 1 ms, 0°
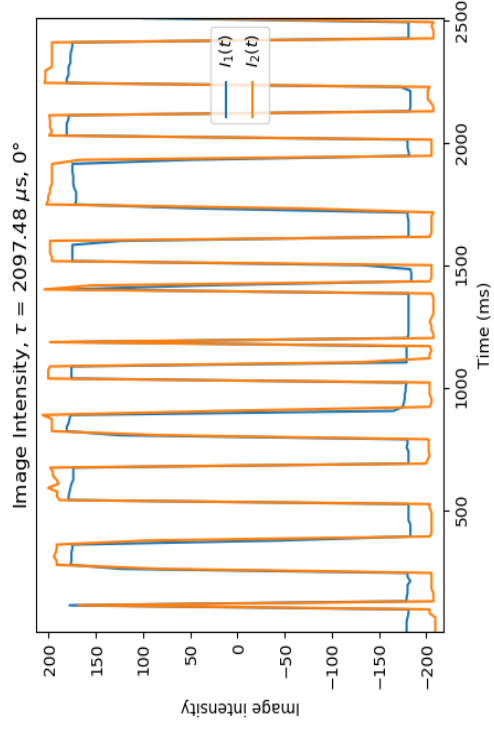
(b) Image intensity of 2 ms, 0°

Figure 4.1: Image intensity for 1 ms and 2 ms at 0°, from 0 to 2.5 s. The intensity from the light from source 1, $I_1(t)$ is given with the orange line, while the intensity from the slightly time-shifted signal from source 2, $I_2(t)$, is given with the blue line.

(a) Image intensity of 10 ms, 0°

(b) Image intensity of 500 μs, 0°

Figure 4.2: Image intensity for 10 ms and 500 μs at 0°, from 0 to 2.5 s. The intensity from the light from source 1, $I_1(t)$ is given with the orange line, while the intensity from the slightly time-shifted signal from source 2, $I_2(t)$, is given with the blue line.
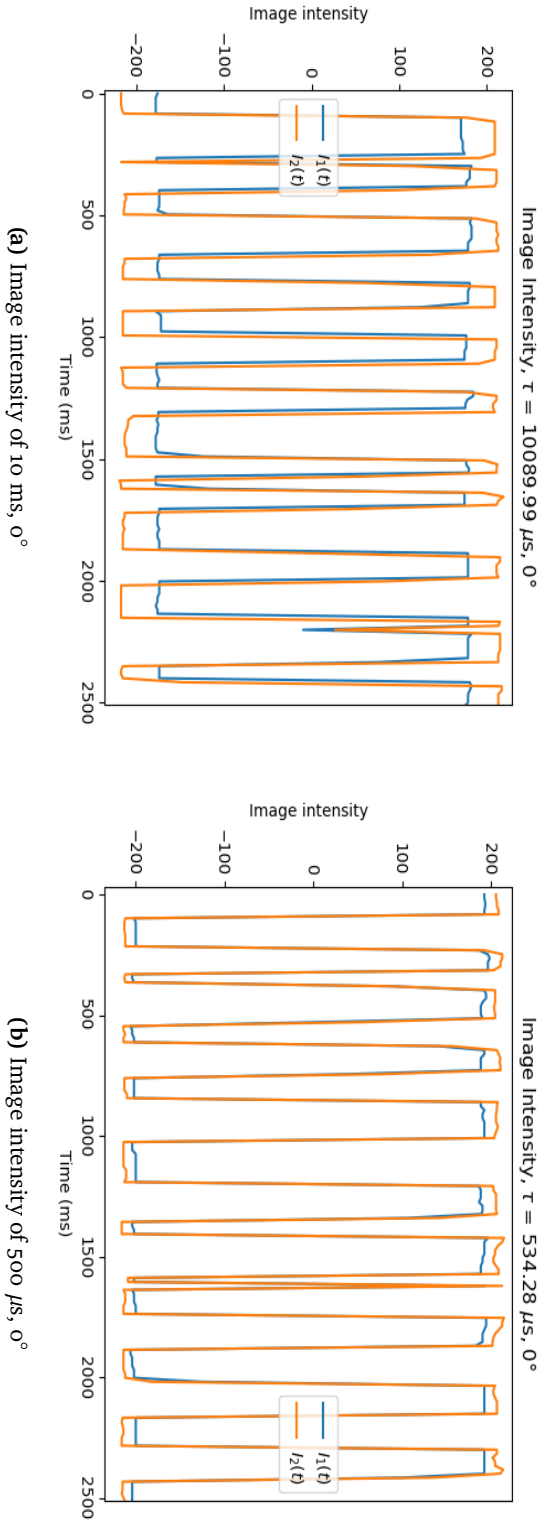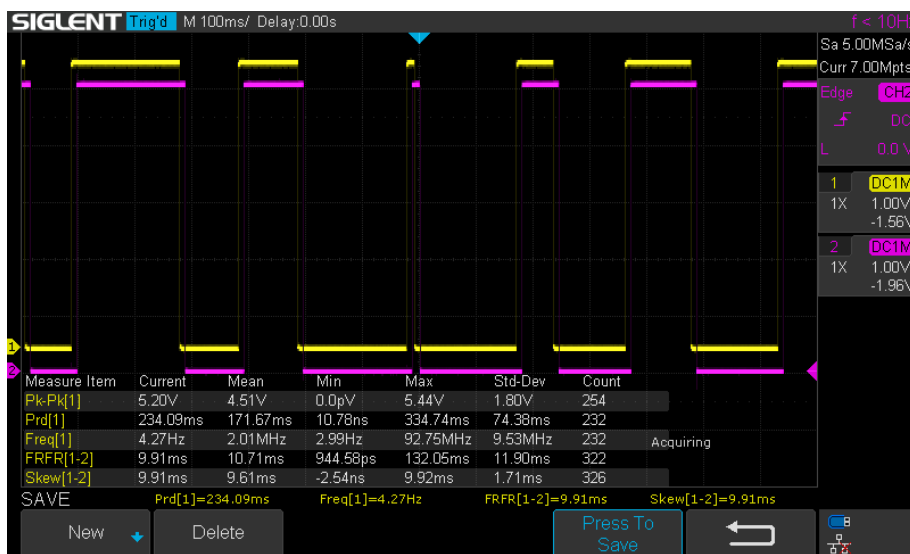
Figure 4.3: Oscilloscope measurement of $\tau = 10$ ms. The Figure shows small jitters between the signals.

Figure 4.1 to 4.2 shows how the intensity of the both source 1 and source 2 varies when there is a random on-off pulse-lengths between the sources. This plot only shows time delays between 0 s and 2.5 s.

Figure 4.4 show the estimated cross-spectral power for a 10 minute recording of signals $I_1(t)$ and $I_2(t)$ with τ from 1, which are the true values, at an angle of 0°. Other cross-spectral power plots is not shown as they all describe the same. Power is shown in decibel (dB) units. The spectral power is mostly centered around low frequencies, about 5 Hz, and gradually decreases at frequencies above. This is intentional, as it is important to reduce aliasing effects, which can cause unexpected phase behaviour. In this case, the DC component has been removed as it does not give any information about the time delay, as the cross-phase is equal to zero here. The cross-spectral phase measurements for 10 minute recordings of the calibrator source are also given in Figure 4.5 to 4.12. The plots on the left show the cross-phase. when making the measurements, 40 neighbouring cross-spectral components are obtained using Fourier transforms of signals $I_1(t)$ and $I_2(t)$. Signals $I_1(t)$ and $I_2(t)$ were selected as intensity values of single pixels, as specified earlier in this section. The central part of the cross-spectra follows a linear slope as shown from Equation 3.7. This linear slope provides information about the time delay. The edges of the cross-spectra phase do not follow the linear slope, of which the reason is uncertain. This is likely to be a combination of either aliased signals due to low spectral power on higher frequencies, or due to video compression. While the plots on the left shows the fit residuals between the best fit and the fitted measurements

between 0 and 10 Hz.

The linear part of the cross-spectral phase is used to fit for the time delay. All of these fits were within 100 μs of the true time delay that the calibration device was set to. Except for the $\tau = 10$ ms, 180° measurement where the measured time delay exceeds 100 μs.
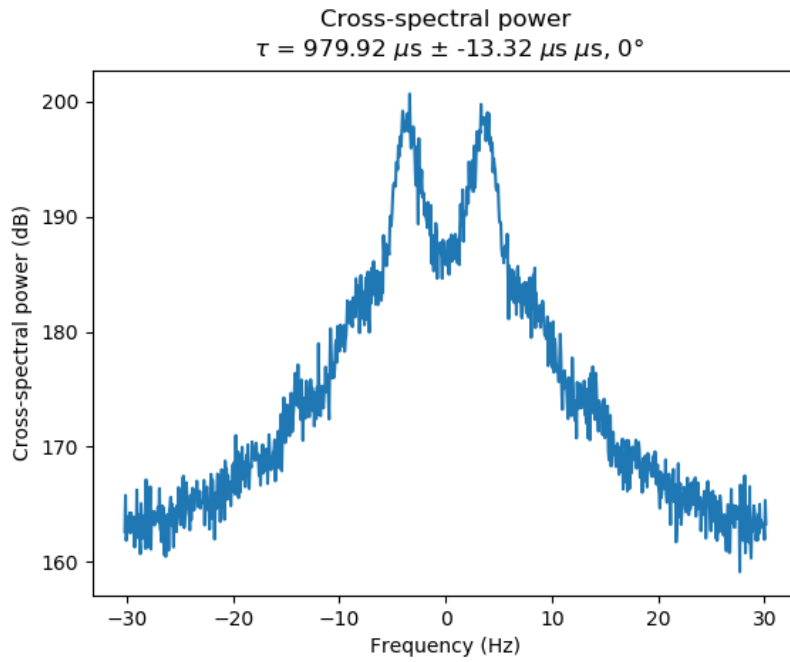

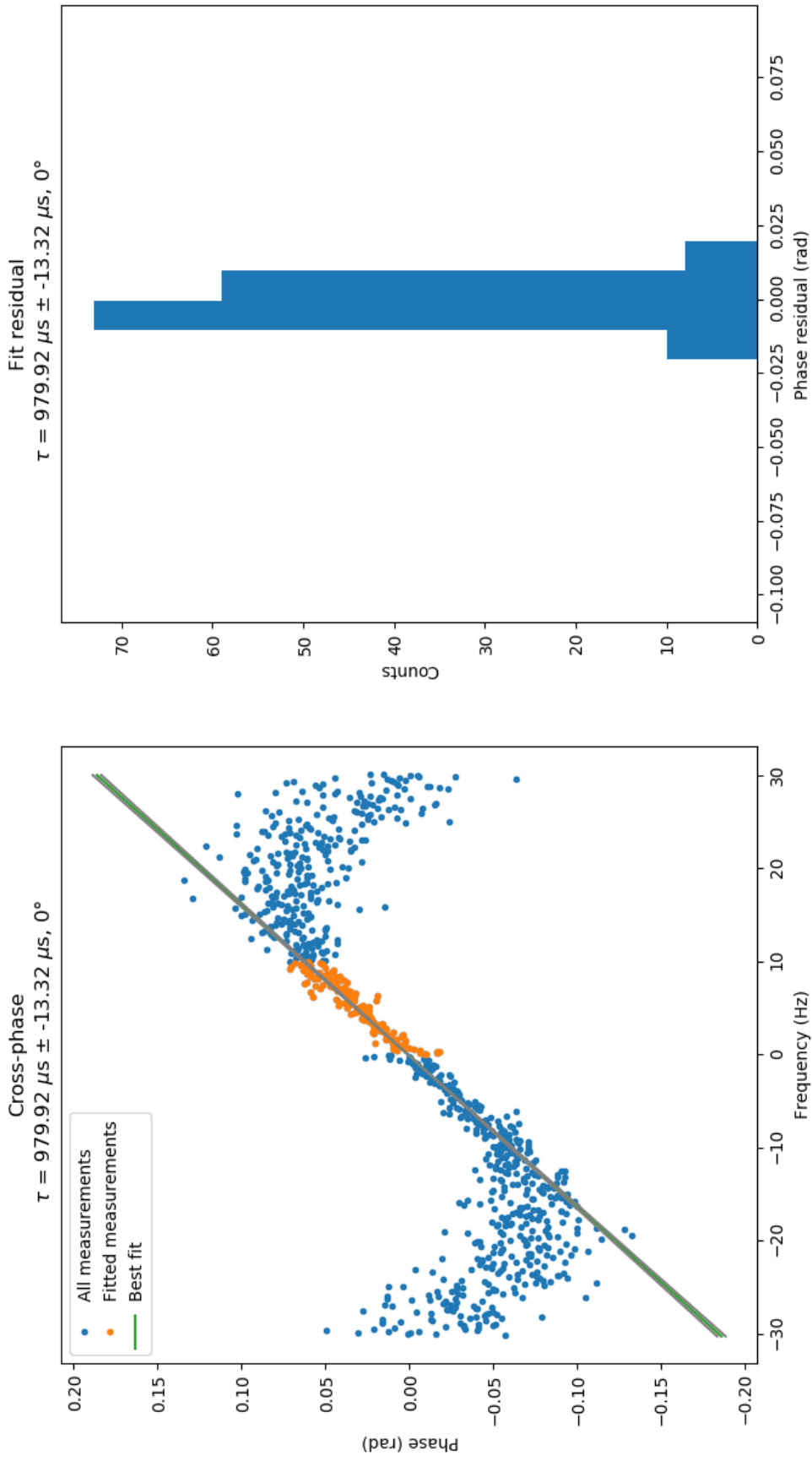**Figure 4.4:** Cross-spectral power for 1 ms, 0° corresponding a 10 minute recording of a calibration signal

Figure 4.5: Cross-phase and Fit residual between the best fitted line (green) and the fitted measurements between 0 and 10 Hz for $\tau = 1$ ms, 0°

Figure 4.6: Cross-phase and Fit residual between the best fitted line (green) and the fitted measurements between 0 and 10 Hz for τ = 2 ms, 0°.

Figure 4.7: Cross-phase and Fit residual between the best fitted line (green) and the fitted measurements between 0 and 10 Hz for τ = 10 ms, 0°
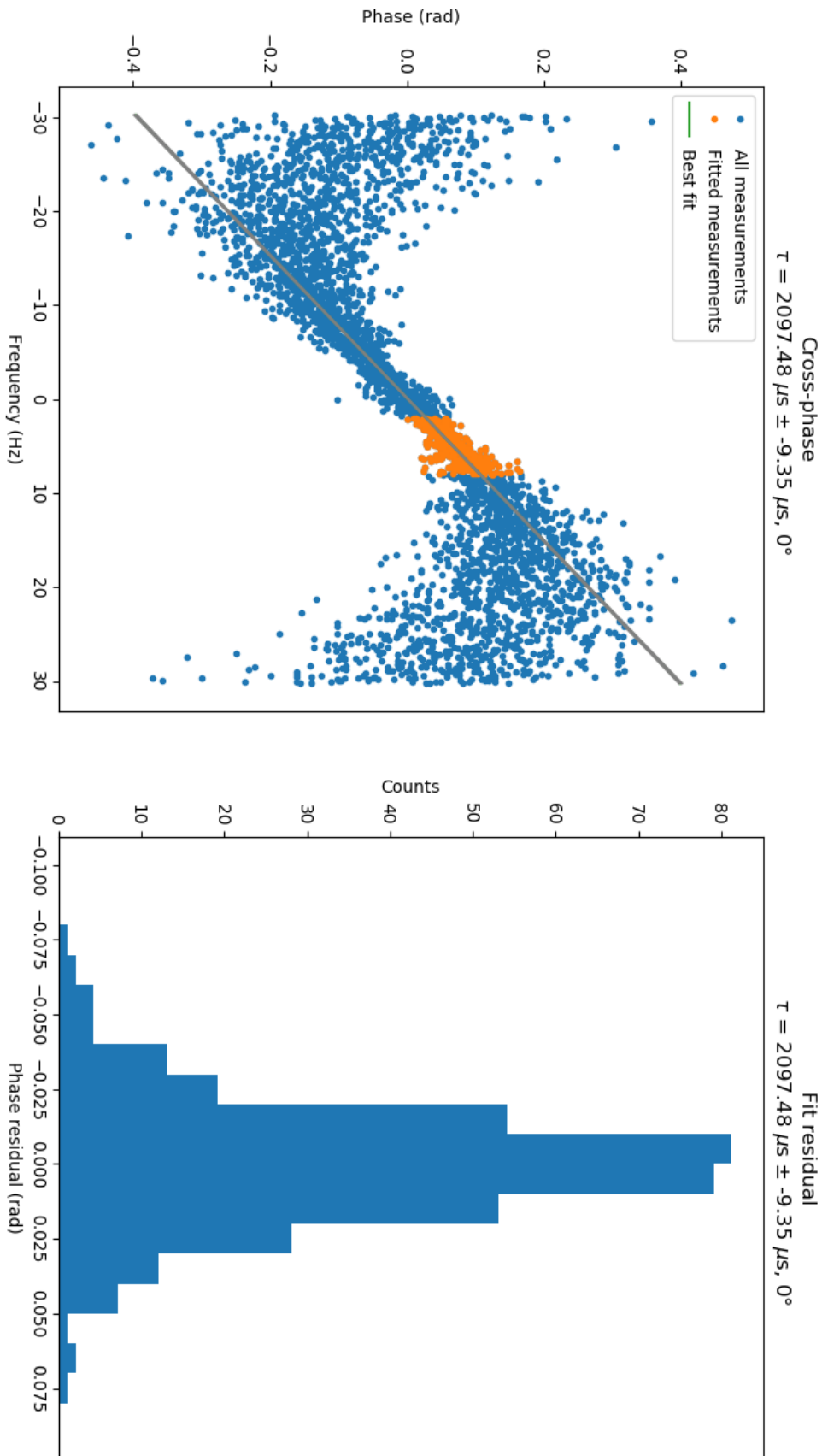
Figure 4.8: Cross-phase and Fit residual between the best fitted line (green) and the fitted measurements between 0 and 10 Hz for $\tau = 500$ μs, $0°$

Figure 4.9: Cross-phase and Fit residual between the best fitted line (green) and the fitted measurements between 0 and 10 Hz for $\tau = 1$ ms, 180°

Figure 4.10: Cross-phase and Fit residual between the best fitted line (green) and the fitted measurements between 0 and 10 Hz for $\tau = 2$ ms, 180°.
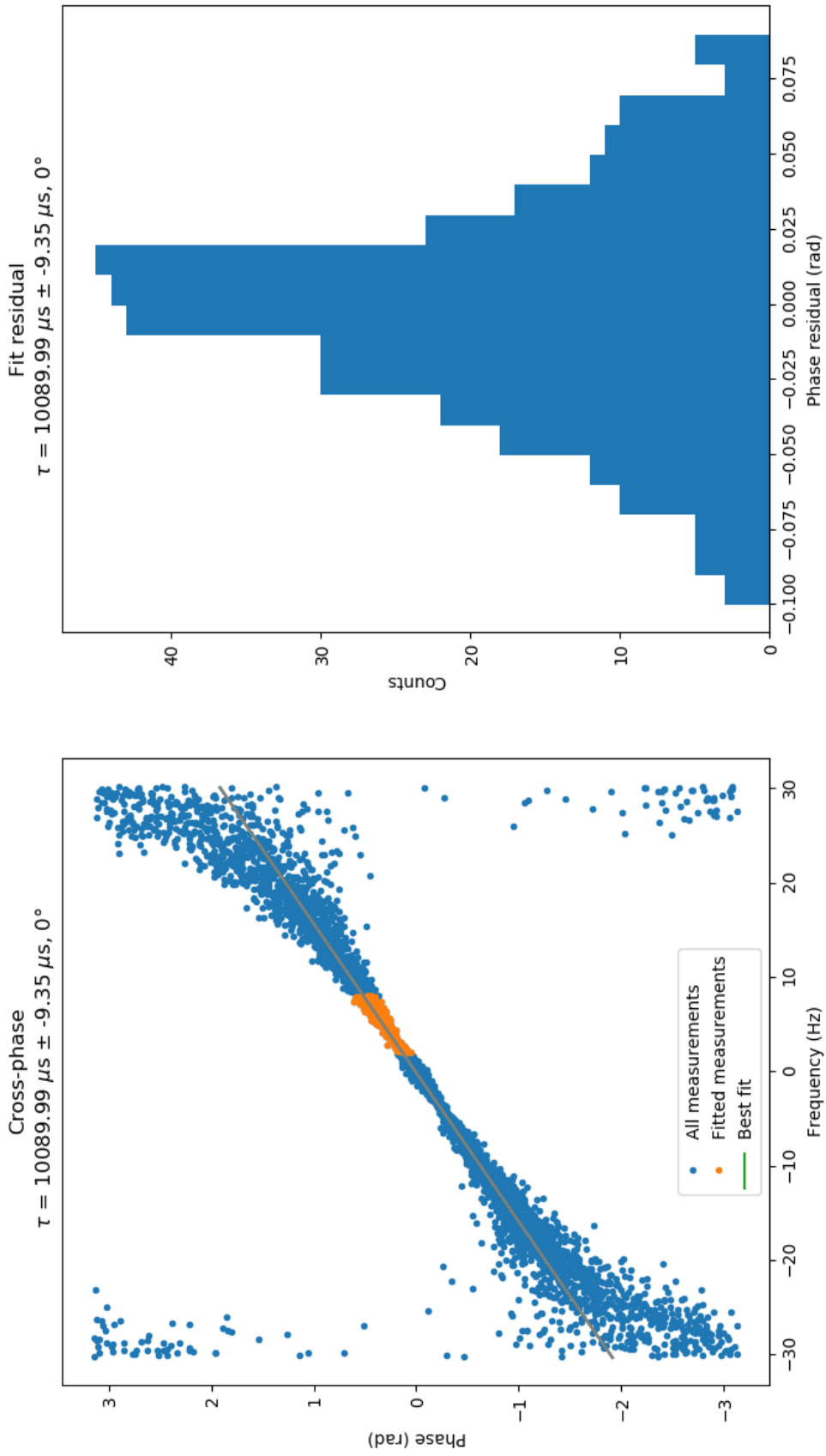
Figure 4.11: Cross-phase and Fit residual between the best fitted line (green) and the fitted measurements between 0 and 10 Hz for τ = 10 ms, 180°
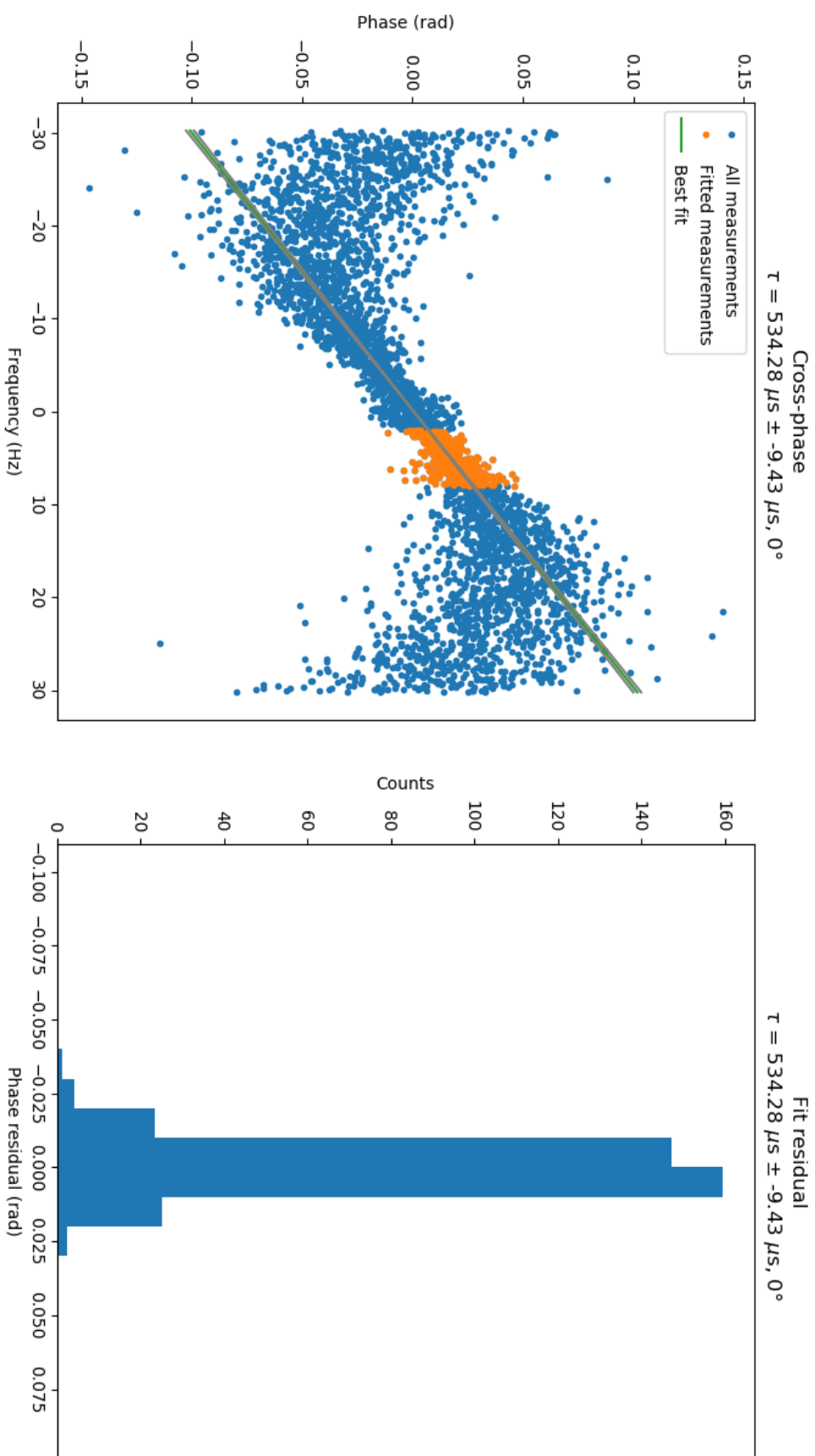
Figure 4.12: Cross-phase and Fit residual between the best fitted line (green) and the fitted measurements between 0 and 10 Hz for $\tau = 500$ μs, 180°.

Figure 4.13: Cross-phase and Fit residual between the best fitted line (green) and the fitted measurements between 0 and 10 Hz for $\tau = 1$ ms, 90°

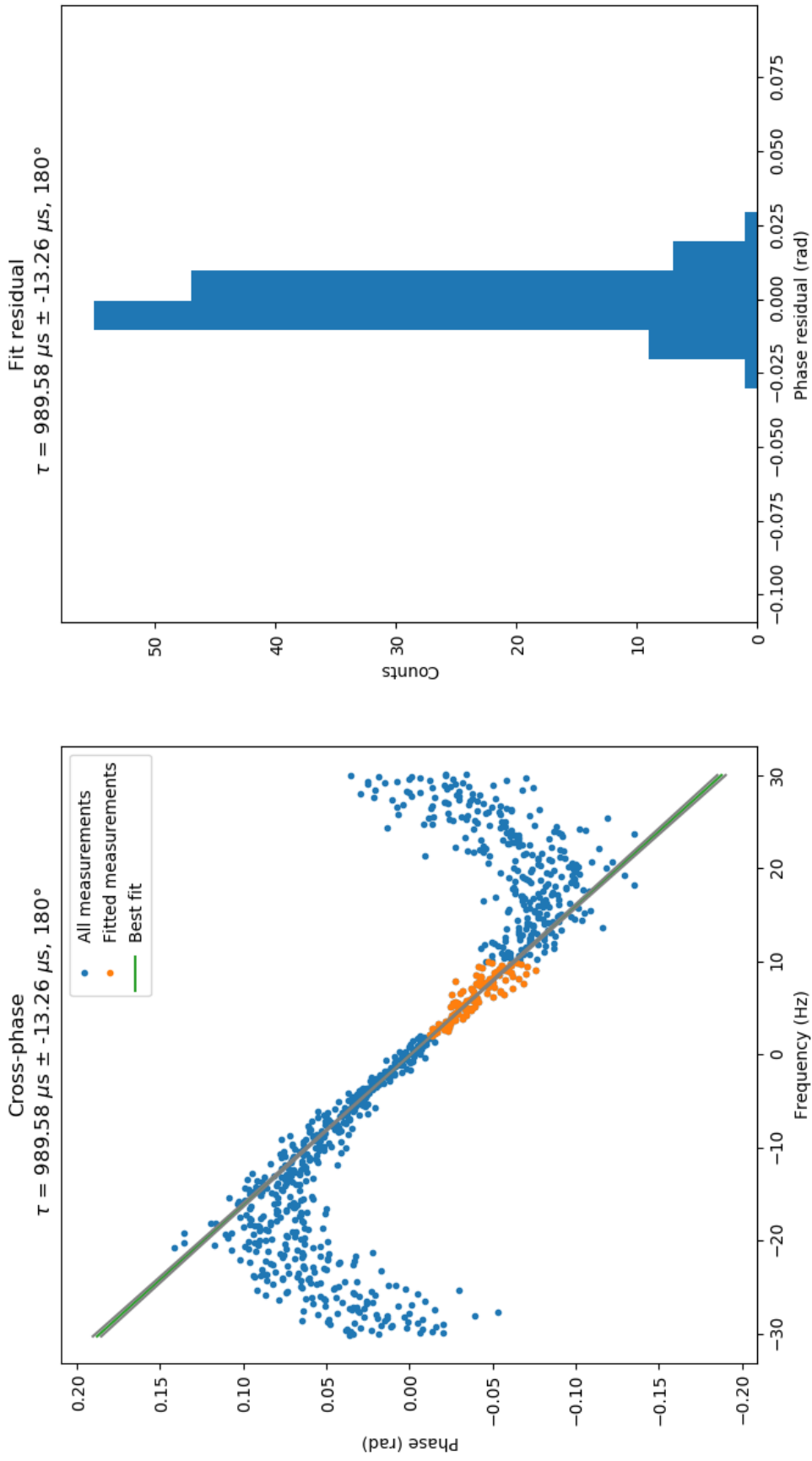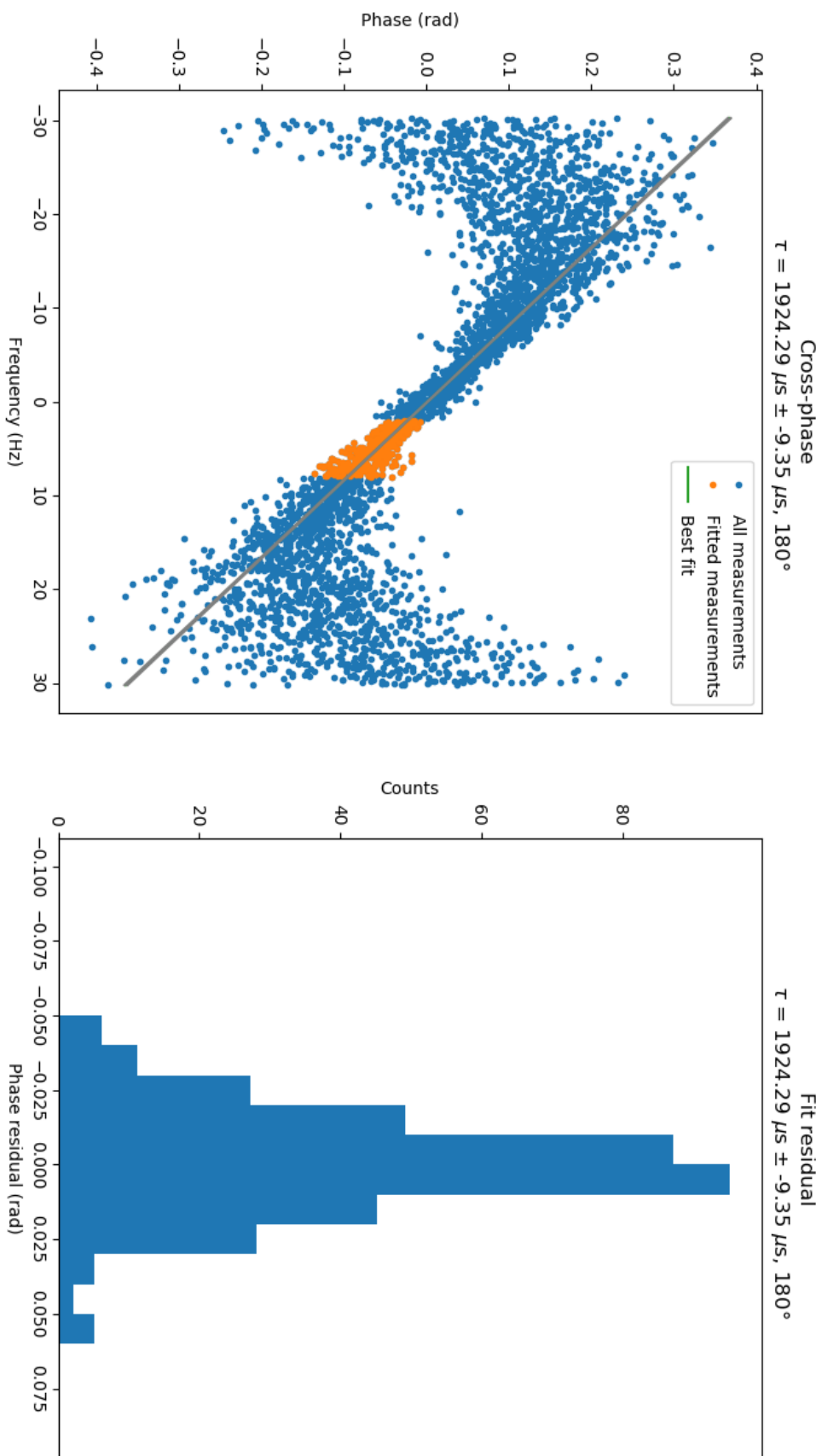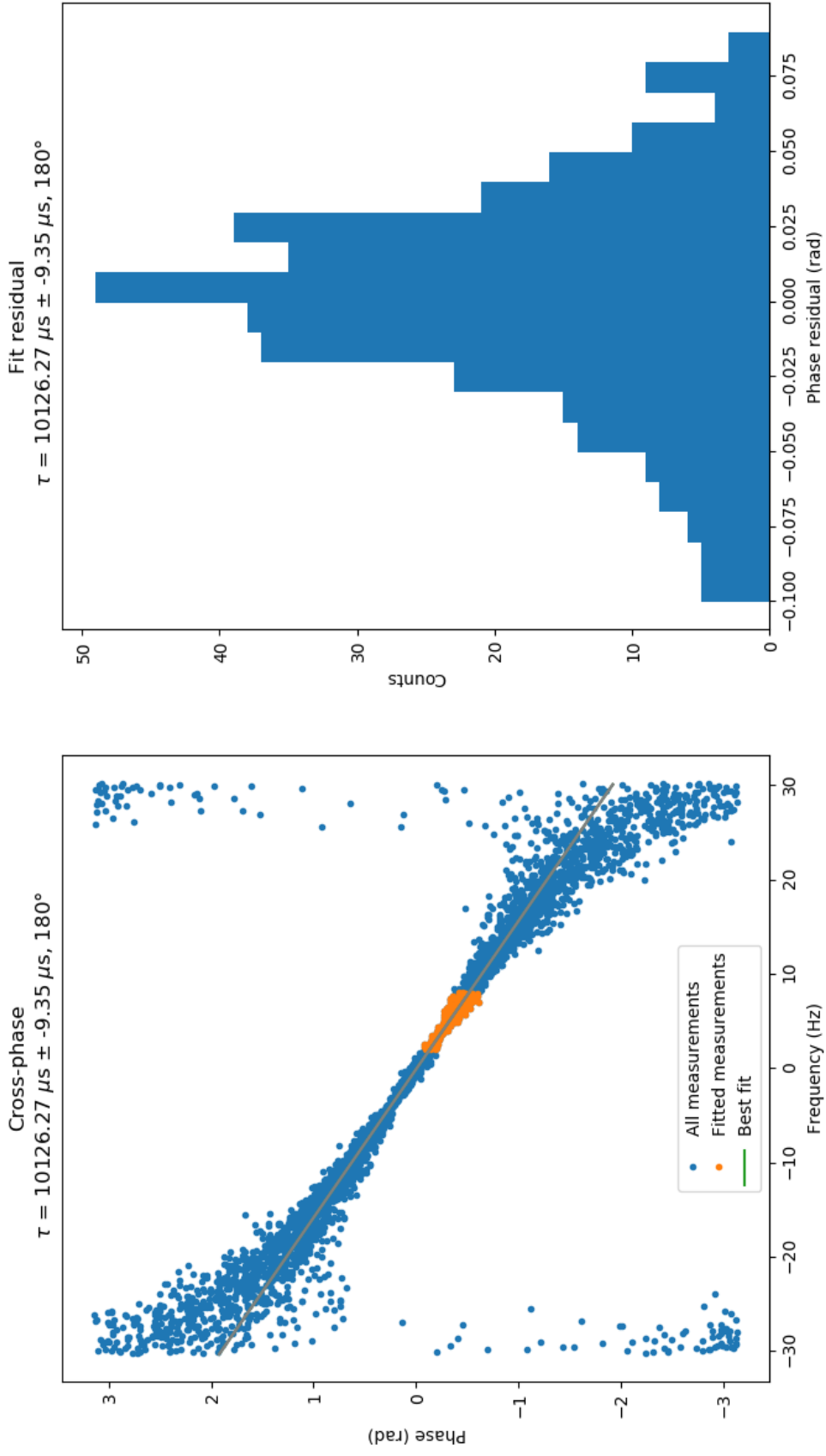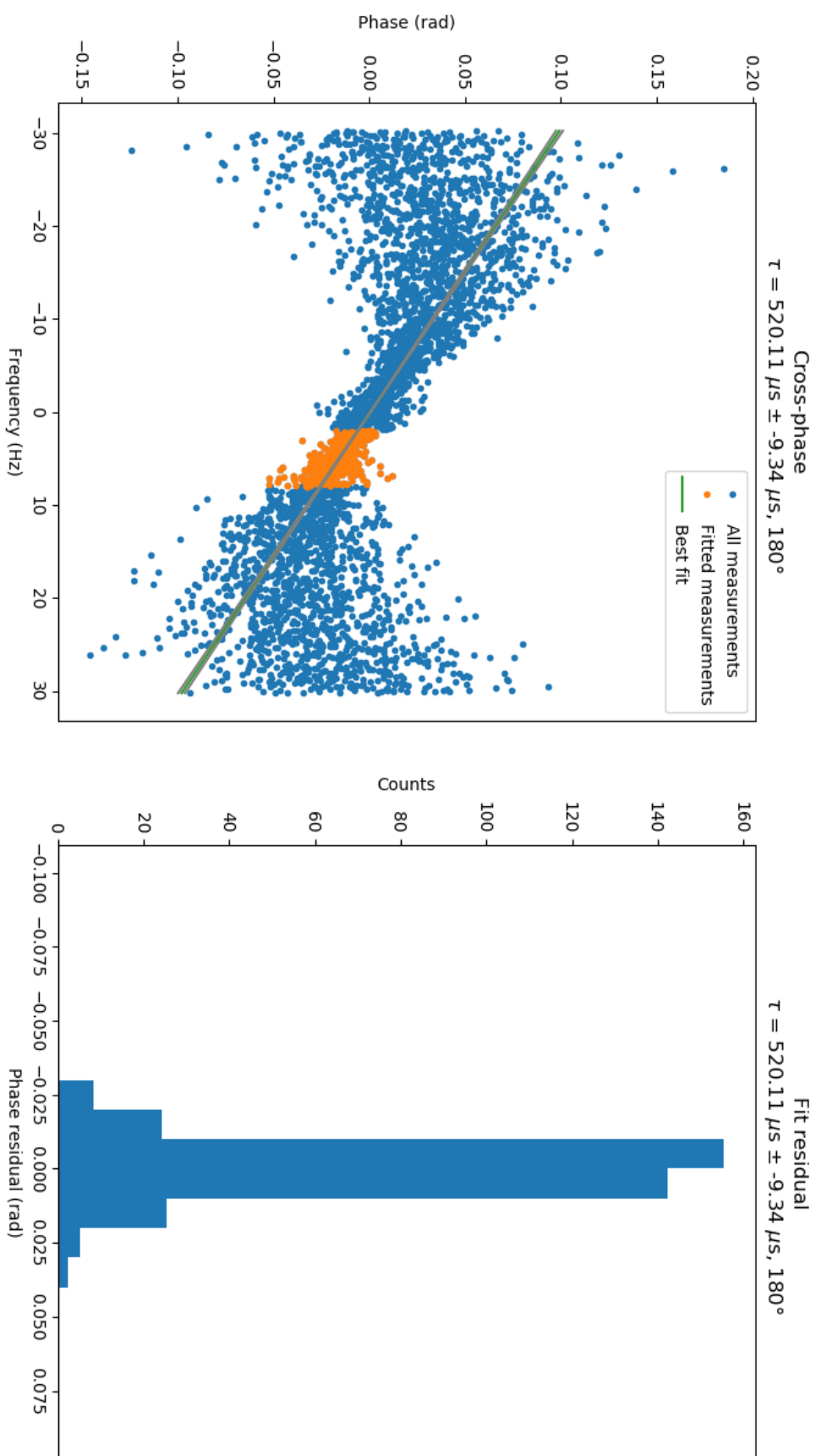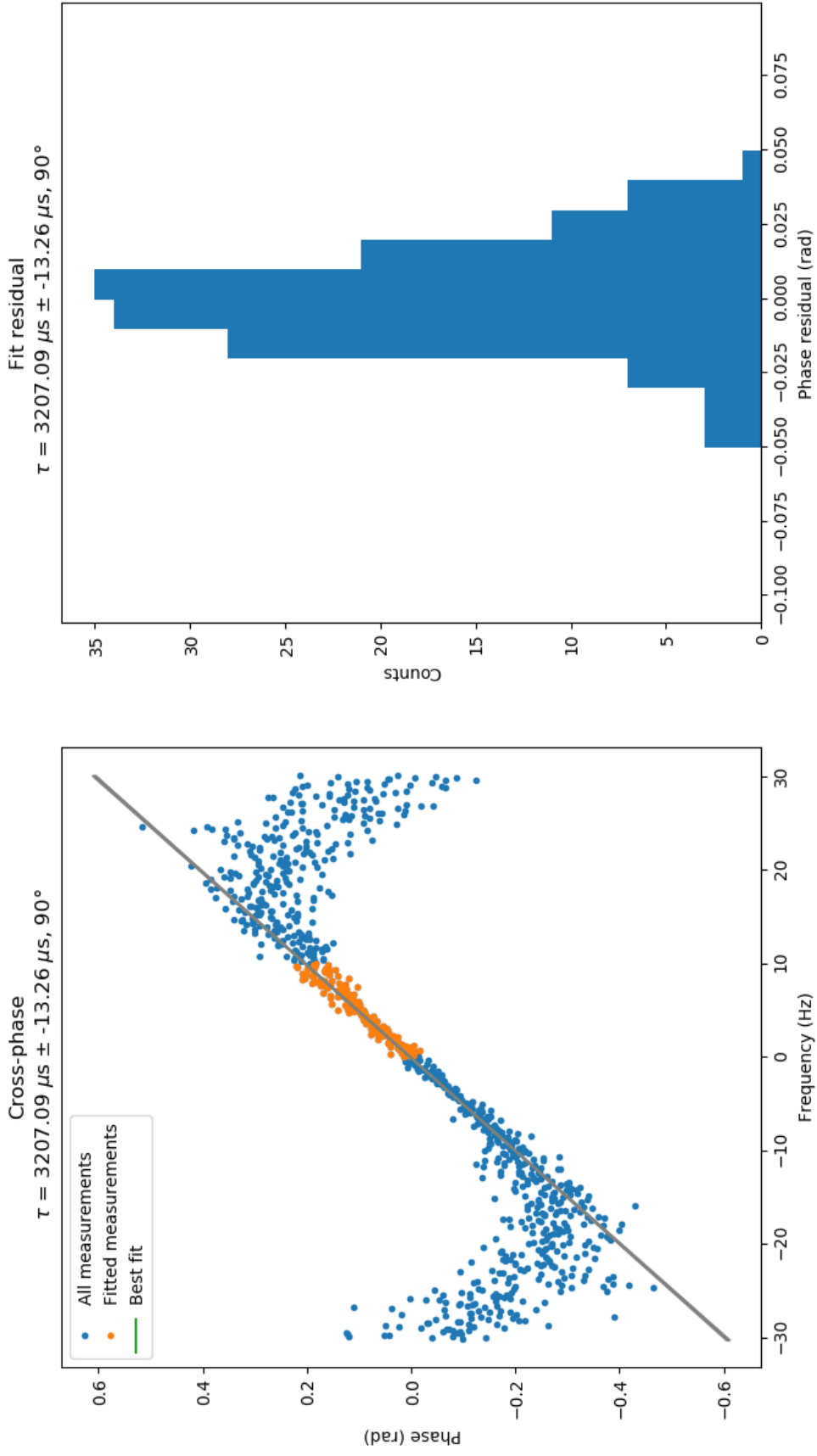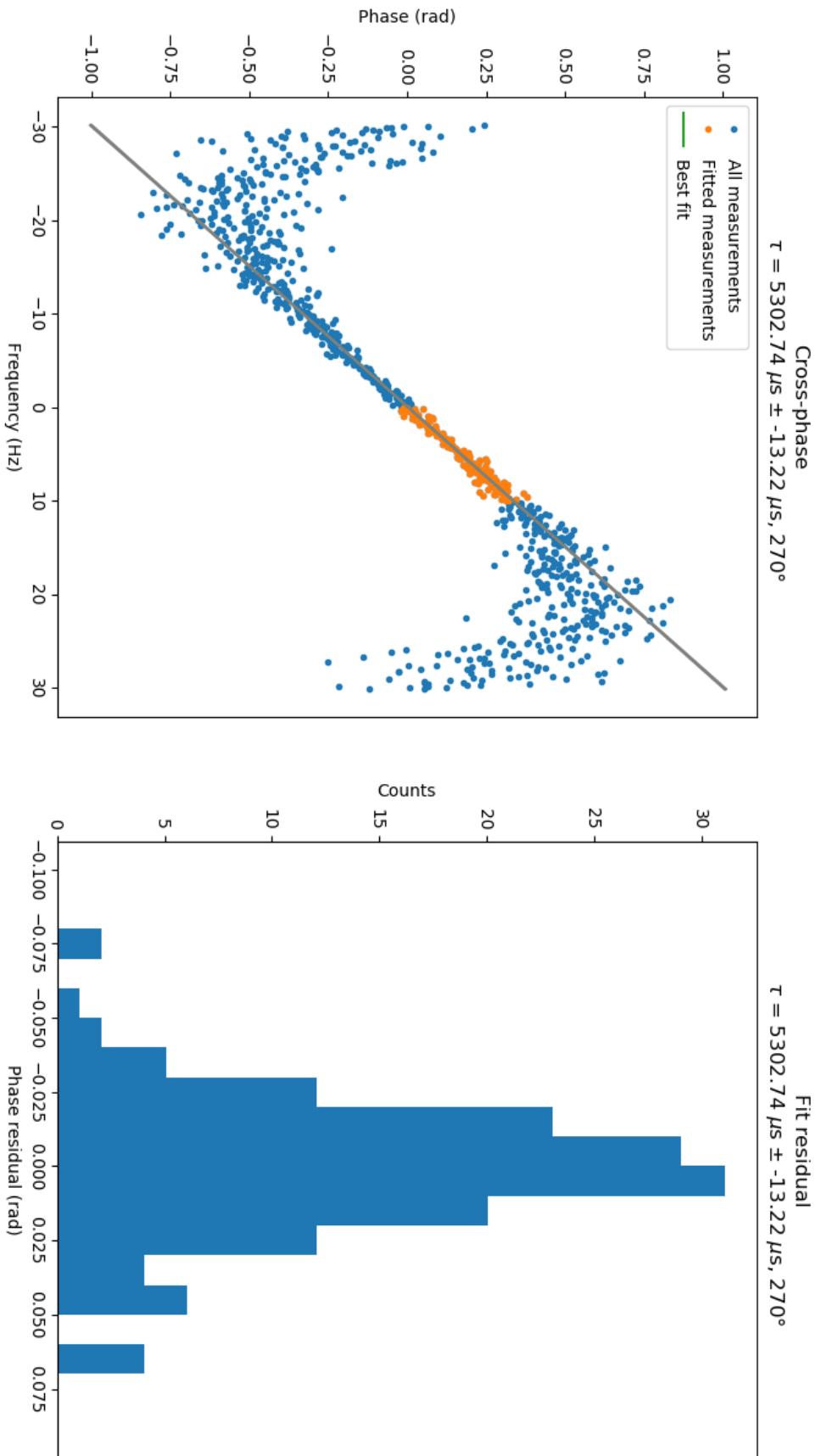**Figure 4.14:** Cross-phase and Fit residual between the best fitted line (green) and the fitted measurements between 0 and 10 Hz for $\tau = 1$ ms, 270°.

In order to characterize error behaviour as a function of measurement time span, a series of measurements with different analysis time spans was conducted, followed by an estimation of the error standard deviation of the estimated time delay. These are given in Table 4.2 and 4.3. The phase measurement error variance was estimated using a sample average estimate based on the maximum likelihood fit residual. All spectral components with frequencies between 0 and 10 Hz were used to fit the time delay, while negative spectral components were not used to ensure that the errors are uncorrelated. The estimated time delays, orientation of the calibration devices, measurement time spans, number of frames, estimated time delays, and true delay estimation errors are given in Table 4.2 and 4.3. The tables show that the estimation error standard deviation is reduced when the measurement length is increased. The estimated time delays are less than $2\sigma_\tau$ from the true value of the time delay in all cases, but in most cases larger than the time delay uncertainties. Hence, the time delay estimation error standard deviation is slightly underestimated. The reason for this might be due to lower quality measurements of the cross-spectral phase at higher frequencies, but this is uncertain. Some artefacts due to video compression are possible.

Table 4.2: Measurement of time-shift for different time spans. The measurements that has been conducted uses $\tau = 10$, 2, 1 and 0.5 ms for the time delay. The time duration of the measurement is T, the number of frames analyzed is N_f, the time delay uncertainty is σ_τ, the estimated time shift is τ_m, and the difference between the value and the estimated value is $\tau_m - \tau$. These measurements are only the 0° measurements.

time delay τ (ms)	Rotation (degree)	T (s)	N_f	time delay uncertainty σ_τ (μs)	τ_m (μs)	$\tau_m - \tau$
10	0	5	300	105	8998	-1092
		17	1000	58	10808	718
		50	3000	32	9976	-114
		167	10000	18	10220	130
		606	36346	9	10090	0
2	0	5	300	105	2214	135
		17	1000	58	1830	-249
		50	3000	32	2212	133
		167	10000	18	2077	-2
		605	36309	9	2079	0
1	0	5	300	159	957	-23
		17	1000	71	931	-49
		50	3000	46	942	-38
		167	10000	26	946	-34
		606	36333	13	980	0
0.5	0	5	300	105	328	-206
		17	1000	58	502	-32
		50	3000	32	569	35
		167	10000	18	571	37
		605	36321	9	534	0

Table 4.3: Measurement of time-shift for different time spans. The measurements that has been conducted uses $\tau = 10, 2, 1$ and 0.5 ms for the time delay. The time duration of the measurement is T, the number of frames analyzed is N_f, the estimated time delay uncertainty is σ_τ, the estimated time shift is τ_m, and the difference between the value and the estimated value is $\tau_m - \tau$. These measurements are only the $180°$ measurements.

time delay, τ (ms)	Rotation (degree)	T (s)	N_f	Time delay uncertainty σ_τ (μs)	τ_m (μs)	$\tau_m - \tau$
10	180	5	300	105	9316	-810
		17	1000	58	9640	-486
		50	3000	32	9862	-264
		167	10000	18	9958	-126
		606	36346	9	10126	0
2	180	5	300	105	1274	-650
		17	1000	58	1718	-206
		50	3000	32	1810	-114
		167	10000	18	1874	-50
		605	36309	9	1924	0
1	180	5	300	159	708	-282
		17	1000	71	939	-51
		50	3000	46	966	-24
		167	10000	26	1017	27
		606	36333	13	990	0
0.5	180	5	300	105	539	19
		17	1000	58	504	-16
		50	3000	32	591	71
		167	10000	18	546	26
		605	36321	9	520	0

In order to demonstrate the time delay variation as a function of image pixel-offset a 200×200 pixel region centered on the second light source has been used to estimate the time delay. The pixel regions are given in Table 4.4. The variation of time delays between neighbouring horizontal and vertical pixel direction on the first light source. For each pixel, a time delay was estimated by fitting the cross-spectral phase. 1000 image frames were used due to computer limitations, it was not possible to run for longer time series.

The variation of estimated time delay as a function of images pixel are given in Figure 4.15a to 4.22a. The main effect visible in these figures is the "rolling shutter" effect. Time delay variation between pixels on the same row are relatively similar to one another, but the time delay gradually increases as a function of image row. With a zero vertical pixel offset, the time delays are relatively close to the time delay that the calibration device was configured for.

The distribution of the time delay differences between consecutive pixels are shown in Figure 4.15b to 4.22b. The histogram difference in time delay measurements suggests that the standard deviation of the measurement is less than 10 μs, but the accuracy of this can not be ascertained. From Table 4.2 and 4.3 it is obtained ~18 μs with 10000 image frames, which is quite close to the actual value, when all of the image frames are used.

Table 4.4: Pixel areas that were used to make the measurements. For the 0° and 180° measurements, the pixels on the y-axis were the same, while the x-axis pixels were the same on the 90° and 270° measurements. It was looked at an area of 200×200 to see the pixel offset.

time delay, Δt (ms)	Rotation (degree)	Source 1 pixel (y-axis, x-axis)	Source 2 pixel (y-axis, x-axis)
10	0	(430, 530)	((330, 530), (1800, 2000))
2	0	(350, 550)	((250, 550), (1700, 1900))
1	0	(390, 490)	((290, 490), (1700, 1900))
0.5	0	(250, 350)	((150, 350), (1800, 2000))
10	180	(390, 490)	((290, 490), (1800, 2000))
2	180	(280, 830)	((180, 380), (1900, 2100))
1	180	(260, 360)	((160, 360), (1600, 1800))
0.5	180	(450, 550)	((350, 550), (1700, 1900))

(a) Pixel offset in milliseconds for $\tau = 1$ ms, 0°

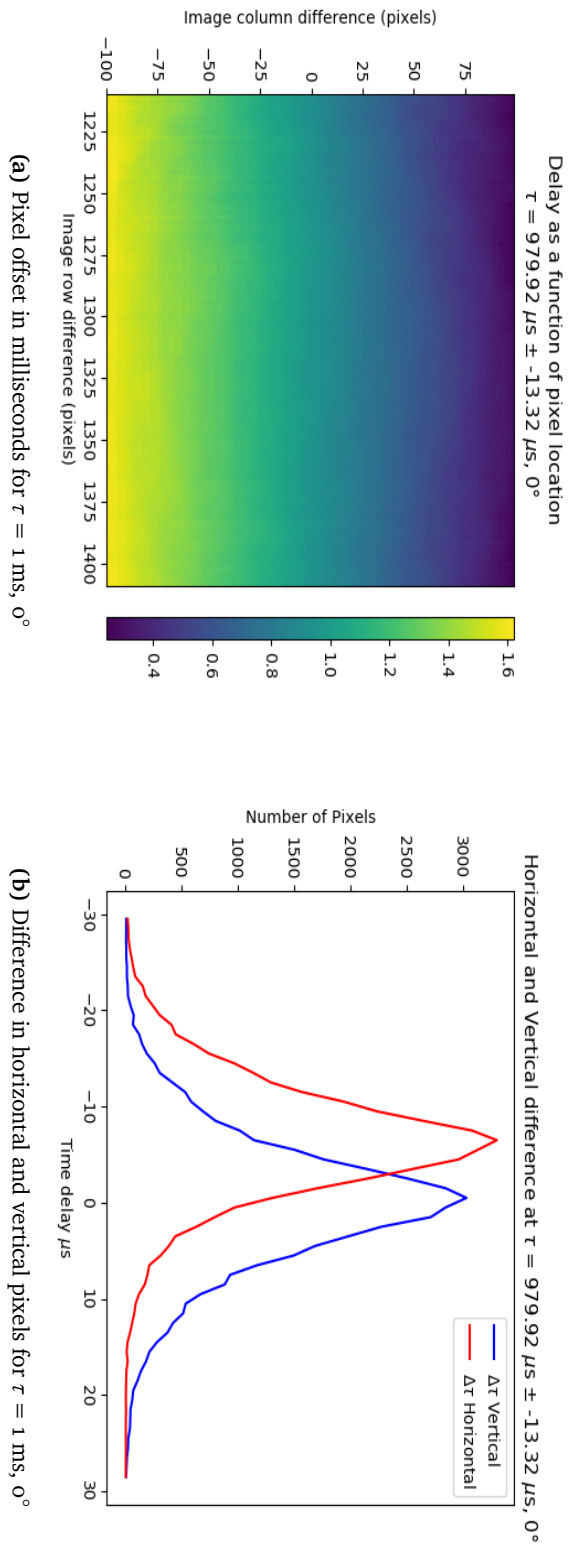**(b)** Difference in horizontal and vertical pixels for $\tau = 1$ ms, 0°

Figure 4.15: time delays, τ, as a function of pixel offset in ms when comparing one pixel from light source 1 and pixels on light source 2 on the left. The linear slope is the effect of the rolling shutter on the smart phone camera used for this test. Zero vertical pixel offset, the time delay close to the 1 ms time delay generated by the calibration device. The distribution of the time delay differences between consecutive pixels are shown on the right.

(a) Pixel offset in milliseconds for $\tau = 2$ ms, 0°

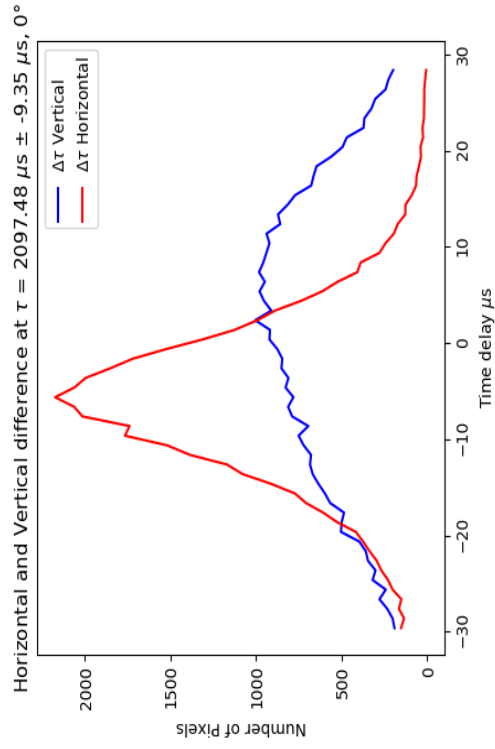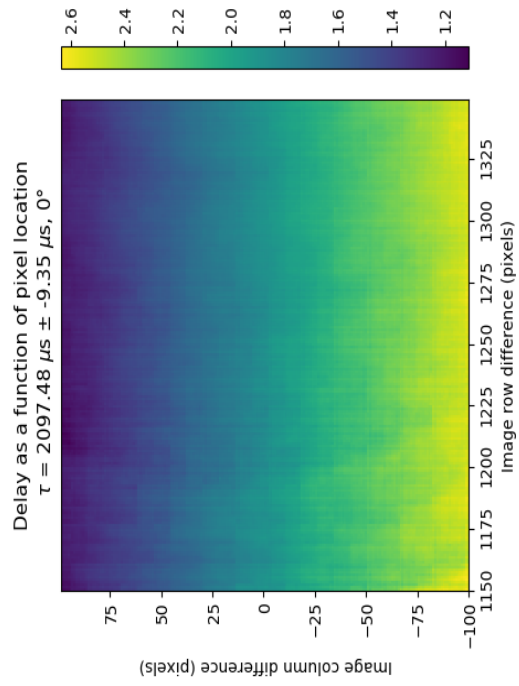(b) Difference in horizontal and vertical pixels for $\tau = 2$ ms, 0°

Figure 4.16: time delays, τ, as a function of pixel offset in ms when comparing one pixel from light source 1 and pixels on light source 2 on the left. The linear slope is the effect of the rolling shutter on the smart phone camera used for this test. Zero vertical pixel offset, the time delay close to the 2 ms time delay generated by the calibration device. The distribution of the time delay differences between consecutive pixels are shown on the right.

(a) Pixel offset in milliseconds for $\tau = 10$ ms, $0°$

(b) Difference in horizontal and vertical pixels for $\tau = 10$ ms, $0°$

Figure 4.17: time delays, τ, as a function of pixel offset in ms when comparing one pixel from light source 1 and pixels on light source 2 on the left. The linear slope is the effect of the rolling shutter on the smart phone camera used for this test. Zero vertical pixel offset, the time delay close to the 10 ms time delay generated by the calibration device. The distribution of the time delay differences between consecutive pixels are shown on the right.
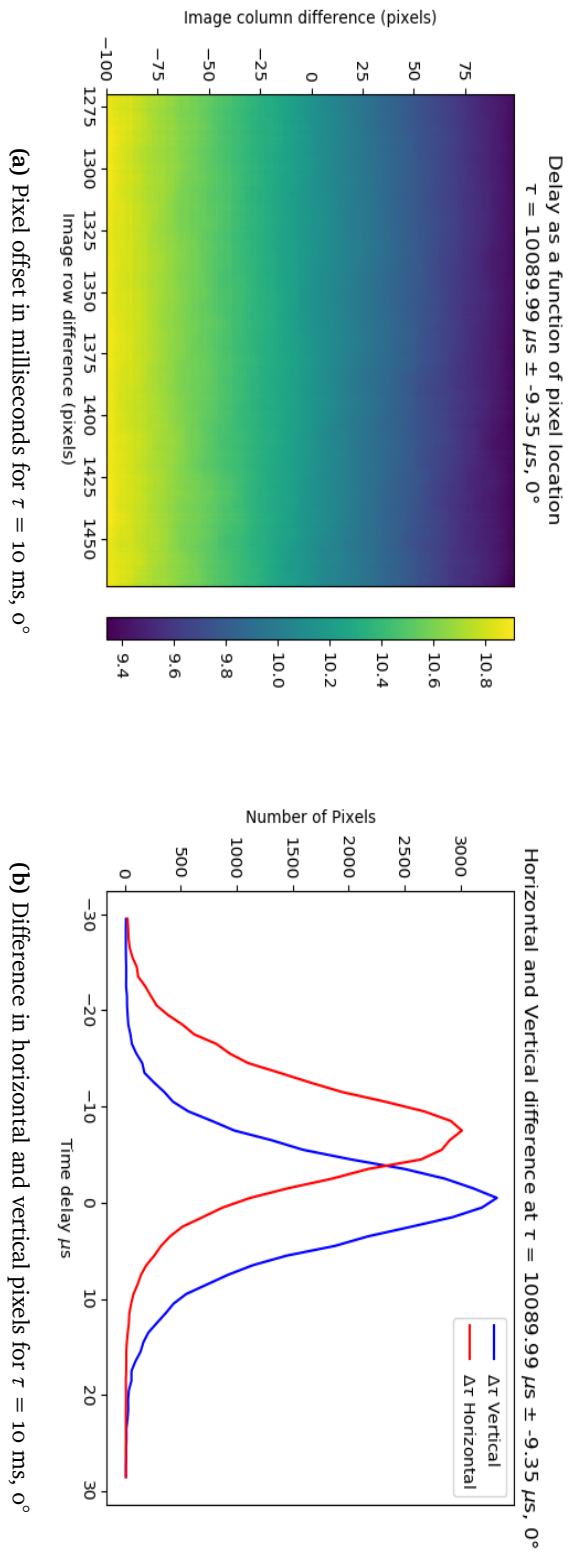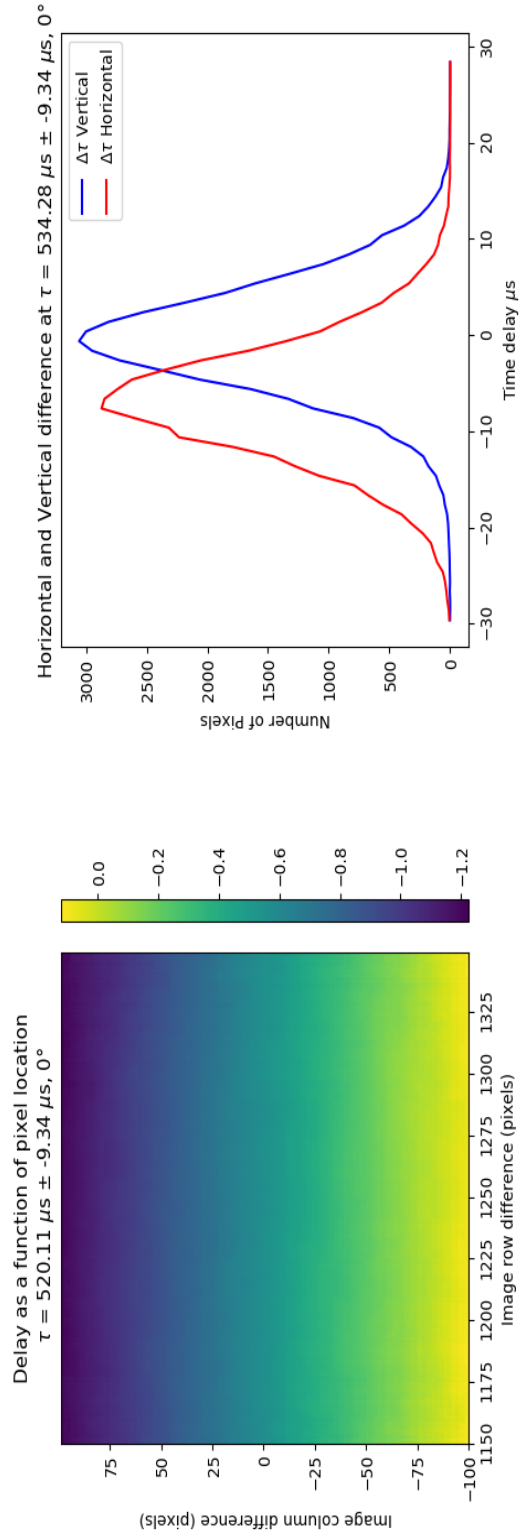
(a) Pixel offset in milliseconds for $\tau = 500 \ \mu s$, 0°

(b) Difference in horizontal and vertical pixels for $\tau = 500 \ \mu s$, 0°

Figure 4.18: time delays, τ, as a function of pixel offset in ms when comparing one pixel from light source 1 and pixels on light source 2 on the left. The linear slope is the effect of the rolling shutter on the smart phone camera used for this test. Zero vertical pixel offset, the time delay close to the 500 μs time delay generated by the calibration device. The distribution of the time delay differences between consecutive pixels are shown on the right.

(a) Pixel offset in milliseconds for $\tau = 1$ ms, 180°

(b) Difference in horizontal and vertical pixels for $\tau = 1$ ms, 180°

Figure 4.19: time delays, τ, as a function of pixel offset in ms when comparing one pixel from light source 1 and pixels on light source 2 on the left. The linear slope is the effect of the rolling shutter on the smart phone camera used for this test. Zero vertical pixel offset, the time delay close to the 1 ms time delay generated by the calibration device. The distribution of the time delay differences between consecutive pixels are shown on the right.
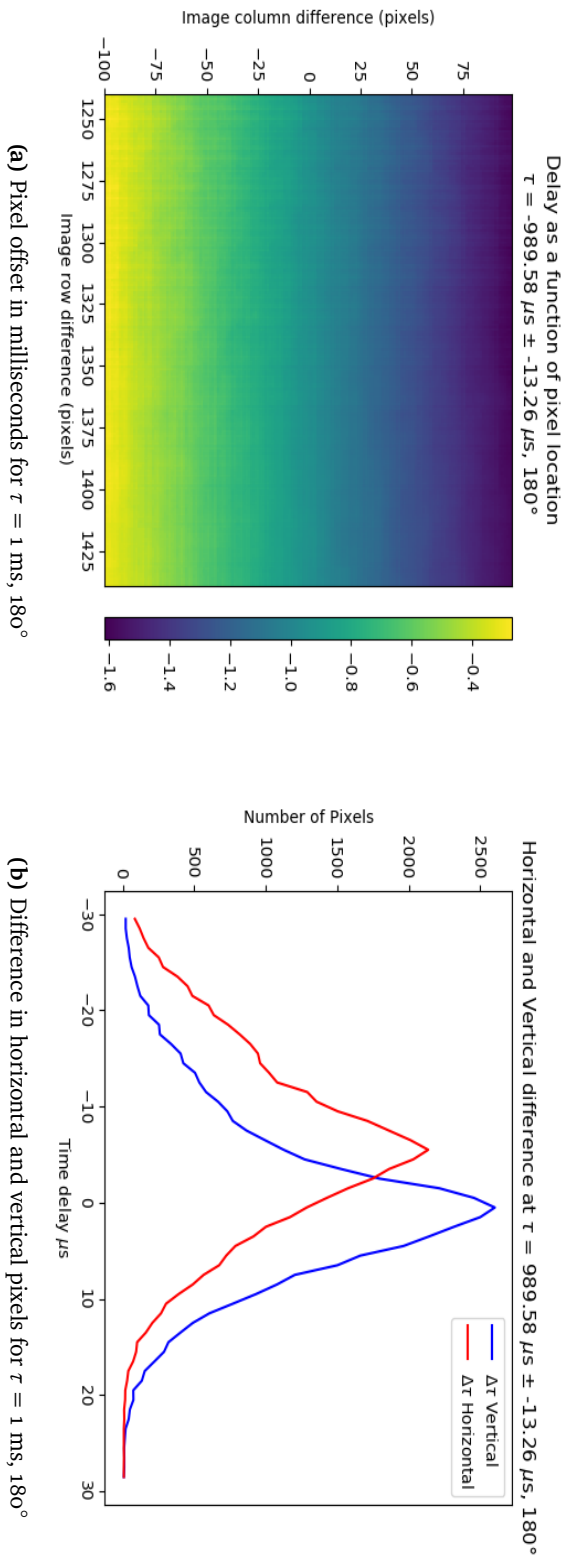
(a) Pixel offset in milliseconds for τ = 2 ms, 180°

(b) Difference in horizontal and vertical pixels for τ = 2 ms, 180°

Figure 4.20: time delays, τ, as a function of pixel offset in ms when comparing one pixel from light source 1 and pixels on light source 2 on the left. The linear slope is the effect of the rolling shutter on the smart phone camera used for this test. Zero vertical pixel offset, the time delay close to the 2 ms time delay generated by the calibration device. The distribution of the time delay differences between consecutive pixels are shown on the right.
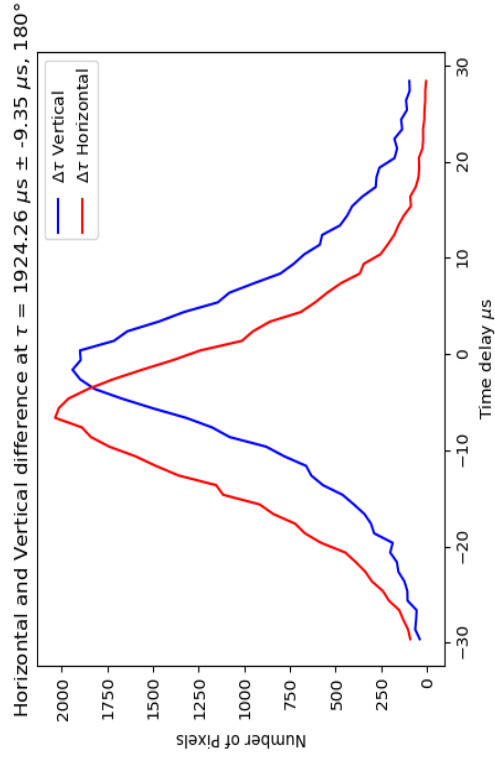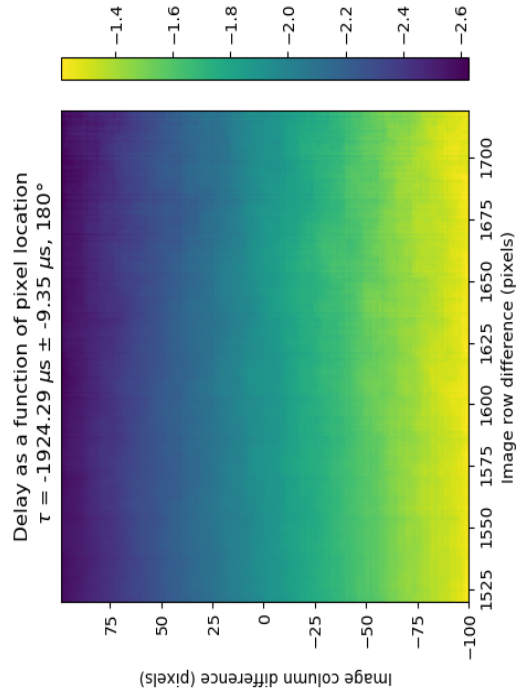
(a) Pixel offset in milliseconds for $\tau = 10$ ms, $180°$

(b) Difference in horizontal and vertical pixels for $\tau = 10$ ms, $180°$
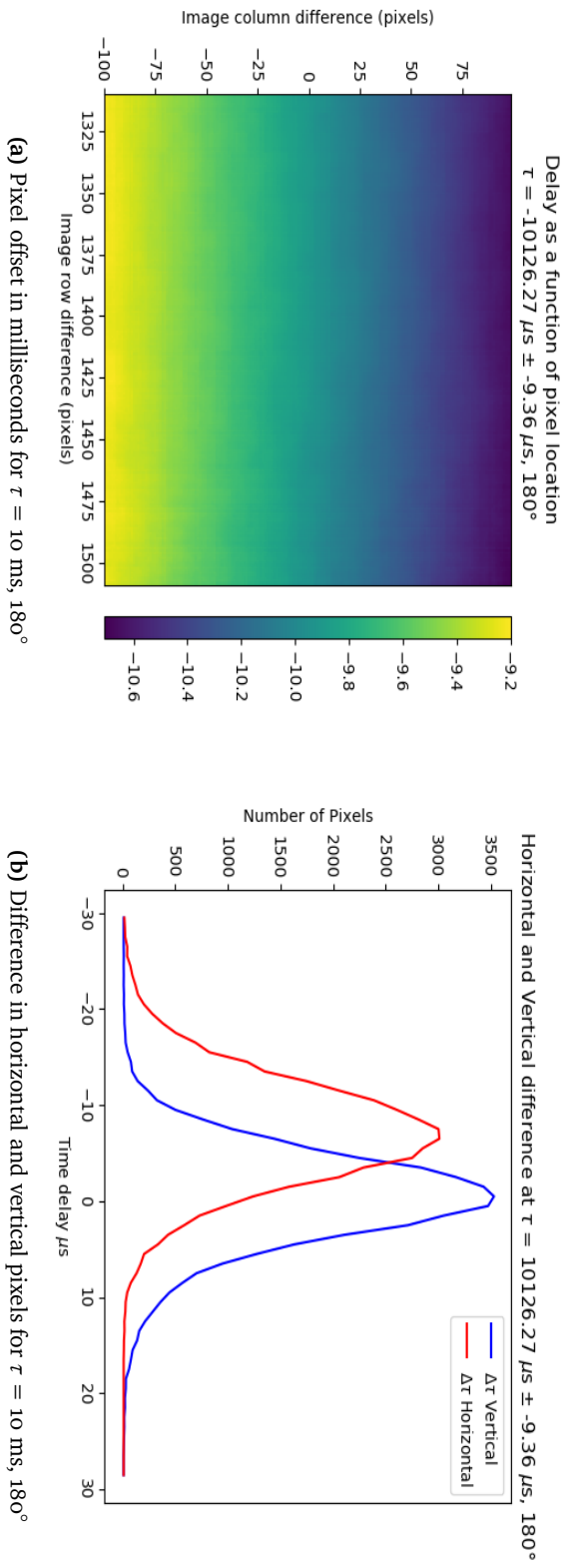
Figure 4.21: time delays, τ, as a function of pixel offset in ms when comparing one pixel from light source 1 and pixels on light source 2 on the left. The linear slope is the effect of the rolling shutter on the smart phone camera used for this test. Zero vertical pixel offset, the time delay close to the 10 ms time delay generated by the calibration device. The distribution of the time delay differences between consecutive pixels are shown on the right.

(a) Pixel offset in milliseconds for $\tau = 500 \ \mu s$, 180°

(b) Difference in horizontal and vertical pixels for $\tau = 1 \ \mu s$, 180°

Figure 4.22: time delays, τ, as a function of pixel offset in ms when comparing one pixel from light source 1 and pixels on light source 2 on the left. The linear slope is the effect of the rolling shutter on the smart phone camera used for this test. Zero vertical pixel offset, the time delay close to the 500 μs time delay generated by the calibration device. The distribution of the time delay differences between consecutive pixels are shown on the right.
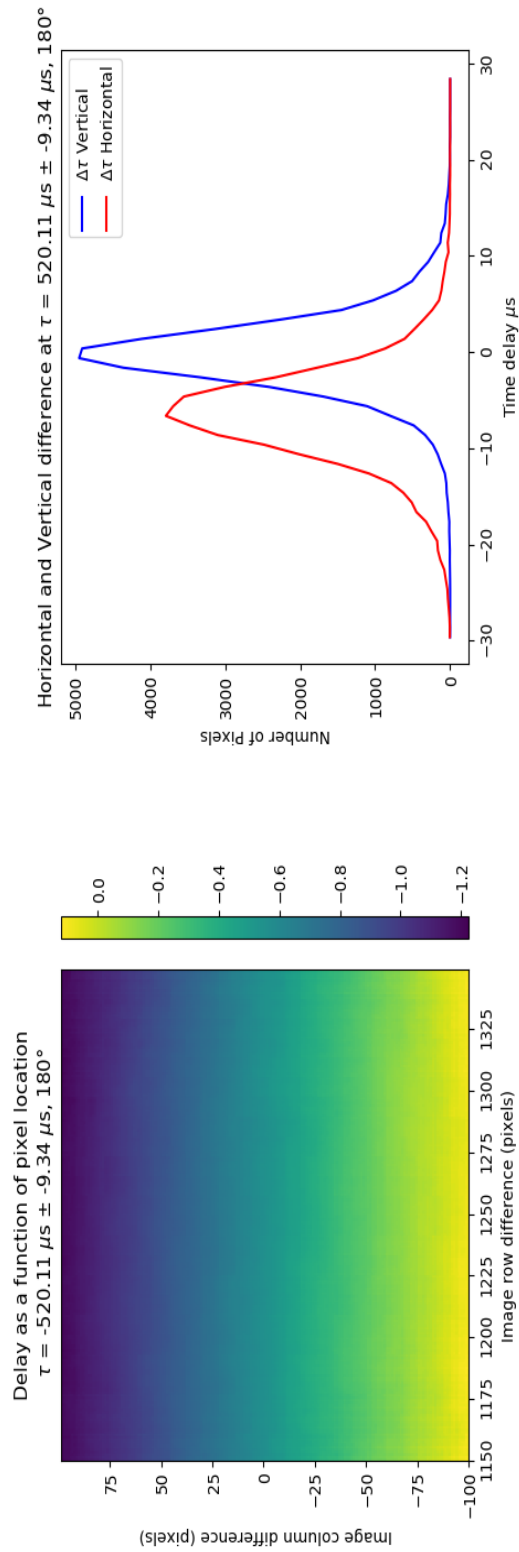
4.1   Discussion

The results shows that the cross-spectral-phase based technique for estimating sub-frame duration with relative time delays between image pixels recorded by a digital video camera works and provide quite accurate measurements of relative pixel-readout time. The target was to obtain time delay-uncertainties in the order of 20 to 50 μs, but this technique produced much better results than expected, as it is obtained time delay accuracies that are better than 10 μs. From the tests that were conducted, it has been demonstrated that this measurement technique will solve the camera synchronization problem with the required accuracy and precision for any future fast moving auroral studies as there is needed a synchronization uncertainty between 1 ms and 100 μs for capturing fast moving auroras.

The image intensity-profiles of the measurements given in 4.1 to 4.2 shows the randomness that was instructed for the microcontroller. The image intensity shows that the intensity of $I_1(t)$, from source 1, is slightly different than the intensity of $I_2(t)$, from source 2. The intensity is also slightly shifted in time. The random pulse-length was introduced to give a power at a wide frequency range. This was also tested on an oscilloscope to ensure that the simulated results were correct.

Since it was established that the image readout orientation with image-row-readout it was utilized data recorded such that the time delay τ could be estimated from pixel imaging of source 1 and source 2 from the same row, i.e. rotations of 90° and 270°. More of the 90° and 270° measurements were not used is because the pixels were read for each row horizontally, such that the 90° and 270° tests yielded much higher pixel readout time than the 0° and 180°, but they gave the same time delay uncertainties, τ. The cross-spectral power and cross-spectral phase for the 90° measurement can be seen in Figure 4.13. The test was executed for $\tau = 1$ ms, but the measured τ shows that the value is almost 3.2 times as high. This is because of the pixel reading were read along the horizontal direction and not the vertical direction. The pixels that were chosen for this measurement were source 1 = (857, 1077) source 2 = (200,1077), where the pixels on the x-axis was the same. The results show that the cross-spectral power is acting as expected, where it decreases as the frequency increases and the power is at its peaks at lower frequencies. For the cross-phase the fitted measurements are between $[0, 10]$ Hz, and the measurements become more random when they reach 30 Hz. That might come from aliasing or because of video compression reasons. The same goes for the 270° measurement. The test is also conducted for $\tau = 1$ ms, but shows that the measured value is 5.3 times greater. The pixels that are chosen for this measurement is source 1 = (839, 1112) and source 2 = (172,1112), where the pixels on the x-axis are the same.

For the 0° and 180° measurements the results did not get that kind of error in τ as is being looked at the pixels on the same row horizontally. Many of the measurements give a time delay uncertainties that are <10 μs, which is much better than the 500 to 100 μs that were expected. The results shows a time delay uncertainties of >10 μs when looking at a time shifts of 1 ms, it might come from some video compression reasons, but it is uncertain. The cross-spectral powers are as expected, where the power is at its highest near the lower frequencies and decreases when reaching the bigger frequencies. The cross-phase increases with angular frequencies when looking at the 0° measurement, while it decreases when looking at the 180° measurement. That is because the measurements are opposite of each other, such that it gets negative frequencies for the time delay at the 180° and positive frequencies for the 0 ° measurements. The important thing to note from theses plots is that the slope is increasing or decreasing nicely, except for the high frequency edges which can be seen from Figure 4.9 to 4.12. The fit residuals shows that there are low phase errors between the the best fitted lines and the fitted measurements.

The pixel delays given in Figure 4.15a to 4.22a show the pixel offset in milliseconds when comparing light source 1 and pixels on light source 2. The linear slope in the vertical direction that can be seen in these figures are the effects of the "rolling shutter" on the smart phone camera used in these tests. One pixel from light source 1 compared to a 200 × 200 pixel-area on light source 2 was used to see how the pixel offset affected the time delay, τ. With zero vertical pixel offset, one can see that the time delays are relatively close to their respective time delays that were set on the calibration device. For this analysis, time-series from 10000 image frames were used as the computer could not handle any larger data sets. Figure 4.15b to 4.22 show the distribution of the time delay difference between consecutive pixels. It can be seen that the change in time-shifts between the pixels on the same row is small. Only 1000 image frames were used here as well, and the time shift change from one row to the next is shown to be 6.58 μs in average. It is uncertain if the average of the time shift change could have been any better, as the tests have some limiting factors, such as uncertain video compression.

5

Conclusion

The results show that the proposed method for estimating sub frame duration relative time delays between pixels recorded by a smart phone digital video camera, Huawei P30 Pro, works and provides an accurate measurement of relative time shift between image pixels. This technique can not only be used to estimate synchronization of image sensors, but also to carry out measurements of sub frame resolution time shifts for a spectrally broad image time-series, more specifically, $\tau \sim 500\mu s \pm 15\ \mu s$ with one or more cameras provided that the auroral time-variations are rapid enough.

For this method, and easy and inexpensive calibration device was built for calibrating the camera timing. Two LEDs were used as light sources, one with an intensity of $I_1(t)$ and the second one with a known time delayed intensity of $I_2(t)$ to measure the pixel readout between the lights. By using only one of the light sources, it is ideally possible to generate a zero time delay signal, which can be used for inter-camera and inter-sensor calibrations.

The cross-phase plots show that with long recordings, in this case; 10 minutes, it is possible to estimate the time delay between image pixels with an accuracy better than 100 μs. This is less than the duration of an image frame. The accuracy is also sufficient to measure the rolling shutter timing of image pixels being read by the CMOS or CCD cameras. From the pixel-region test it is safe to say that the standard deviation of the time delay should be less than 10 μs.

The time delays associated with time-variations of electron fluxes have been estimated to be several milliseconds. In this thesis, it has been shown that this method is suitable to measure these time delays within $<100\mu s$ for events with a duration of less than 20 seconds, given that the time variation of the auroral emission has sufficient spectral width, around 10 Hz.

5.1   Future Work

The calibration technique meets the specified requirements for future auroral observations, in which a low-error-multi-camera-synchronization method is needed. A natural step further would be to test this method on real auroral events with optical cameras. This technique also have the potential to be applicable in a broad range of other digital imaging applications for video camera pixel timing. There is also a potential for testing a mechanical rotating shutter system to look at the harmonic case with a periodic frequency, like shown in Figure 5.1:
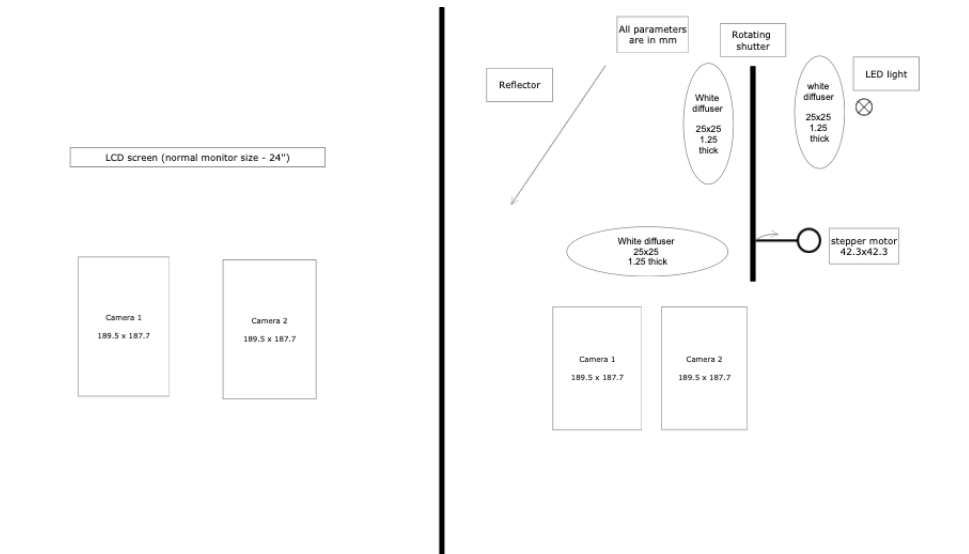

Figure 5.1: A possible blue print for a calibration system for any future work.

Bibliography

Bradley, D., Atcheson, B., Ihrke, I., and Heidrich, W. (2009). Synchronization and rolling shutter compensation for consumer video camera arrays. In *2009 IEEE Computer Society Conference on Computer Vision and Pattern Recognition Workshops*, pages 1–8. IEEE.

Dahlgren, H., Aikio, A., Kaila, K., Ivchenko, N., Lanchester, B., Whiter, D., and Marklund, G. (2010). Simultaneous observations of small multi-scale structures in an auroral arc. *Journal of atmospheric and solar-terrestrial physics*, 72(7-8):633–637.

Gustavsson, B. (2020). Time-dependent electron transport i: Modelling of supra-thermal electron burst modulated at 5-10 hz with implications for flickering aurora.

Henriksen, K. and Egeland, A. (1988). The interpretation of the auroral green line. *Eos, Transactions American Geophysical Union*, 69(29):721–734.

Kataoka, R., Miyoshi, Y., Sakanoi, T., Yaegashi, A., Ebihara, Y., and Shiokawa, K. (2011). Ground-based multispectral high-speed imaging of flickering aurora. *Geophysical research letters*, 38(14).

Lanchester, B., Rees, M., Lummerzheim, D., Otto, A., Frey, H., and Kaila, K. (1997). Large fluxes of auroral electrons in filaments of 100 m width. *Journal of Geophysical Research: Space Physics*, 102(A5):9741–9748.

Sakanoi, K. and Fukunishi, H. (2004). Temporal and spatial structures of flickering aurora derived from high-speed imaging photometer observations at syowa station in the antarctic. *Journal of Geophysical Research: Space Physics*, 109(A1).

Semeter, J. and Blixt, E. (2006). Evidence for alfvén wave dispersion identified in high-resolution auroral imagery. *Geophysical research letters*, 33(13).

Shapiro, I. I. (1976). 5.6. estimation of astrometric and geodetic parameters.

In *Methods in Experimental Physics*, volume 12, pages 261–276. Elsevier.

Šmíd, M. and Matas, J. (2017). Rolling shutter camera synchronization with sub-millisecond accuracy. In *Proc. 12th Int. Conf. Comput. Vis. Theory Appl*, page 8.

Trondsen, T. and Cogger, L. (1998). A survey of small-scale spatially periodic distortions of auroral forms. *Journal of Geophysical Research: Space Physics*, 103(A5):9405–9415.

Vibeck, A. (2015). Synchronization of a multi camera system.

Vogt, J., Frey, H., Haerendel, G., Hofner, H., and Semeter, J. (1999). Papers on magnetospheric physics-shear velocity profiles associated with auroral curls (paper 1999ja900148). *Journal of Geophysical Research-Part A-Space Physics-Printed Edition*, 104(8):17277–17288.

Whiter, D., Lanchester, B., Gustavsson, B., Ivchenko, N., and Dahlgren, H. (2010). Using multispectral optical observations to identify the acceleration mechanism responsible for flickering aurora. *Journal of Geophysical Research: Space Physics*, 115(A12).

Wiegand, T., Sullivan, G. J., Bjontegaard, G., and Luthra, A. (2003). Overview of the h. 264/avc video coding standard. *IEEE Transactions on circuits and systems for video technology*, 13(7):560–576.